The Astrophysical Journal, 954:173 (19pp), 2023 September 10 https://doi.org/10.3847/1538-4357/acddda

The Sloan Digital Sky Survey Reverberation Mapping Project: The Black Hole Mass–Stellar Mass Relations at $0.2 \lesssim z \lesssim 0.8$

Jennifer I-Hsiu Li[1,2,3], Yue Shen[1,4], Luis C. Ho[5,6], W. N. Brandt[7,8,9], Catherine J. Grier[10], Patrick B. Hall[11], Y. Homayouni[7], Anton M. Koekemoer[12], Donald P. Schneider[7,8], and Jonathan R. Trump[13]
[1] Department of Astronomy, University of Illinois at Urbana-Champaign, Urbana, IL 61801, USA
[2] Department of Astronomy, University of Michigan, Ann Arbor, MI, 48109, USA
[3] Michigan Institute for Data Science, University of Michigan, Ann Arbor, MI, 48109, USA
[4] National Center for Supercomputing Applications, University of Illinois at Urbana-Champaign, Urbana, IL 61801, USA
[5] Kavli Institute for Astronomy and Astrophysics, Peking University, Beijing 100871, People's Republic of China
[6] Department of Astronomy, School of Physics, Peking University, Beijing 100871, People's Republic of China
[7] Department of Astronomy & Astrophysics, The Pennsylvania State University, University Park, PA 16802, USA
[8] Institute for Gravitation and the Cosmos, The Pennsylvania State University, University Park, PA 16802, USA
[9] Department of Physics, The Pennsylvania State University, University Park, PA 16802, USA
[10] Department of Astronomy, University of Wisconsin–Madison, Madison, WI 53706, USA
[11] Department of Physics & Astronomy, York University, 4700 Keele St., Toronto, ON M3J 1P3, Canada
[12] Space Telescope Science Institute, 3700 San Martin Dr., Baltimore, MD 21218, USA
[13] Department of Physics, University of Connecticut, 2152 Hillside Rd., Unit 3046, Storrs, CT 06269, USA
Received 2023 January 10; revised 2023 June 6; accepted 2023 June 10; published 2023 September 5

Abstract

We measure the correlation between black hole mass $M_{\rm BH}$ and host stellar mass M_* for a sample of 38 broad-line quasars at $0.2 \lesssim z \lesssim 0.8$ (median redshift $z_{\rm med} = 0.5$). The black hole masses are derived from a dedicated reverberation mapping program for distant quasars, and the stellar masses are derived from two-band optical+IR Hubble Space Telescope imaging. Most of these quasars are well centered within $\lesssim$1 kpc from the host galaxy centroid, with only a few cases in merging/disturbed systems showing larger spatial offsets. Our sample spans two orders of magnitude in stellar mass ($\sim 10^9$–$10^{11}\,M_\odot$) and black hole mass ($\sim 10^7$–$10^9\,M_\odot$) and reveals a significant correlation between the two quantities. We find a best-fit intrinsic (i.e., selection effects corrected) $M_{\rm BH}$–$M_{*,\rm host}$ relation of $\log(M_{\rm BH}/M_\odot) = 7.01^{+0.23}_{-0.33} + 1.74^{+0.64}_{-0.64}\log(M_{*,\rm host}/10^{10}M_\odot)$, with an intrinsic scatter of $0.47^{+0.24}_{-0.17}$ dex. Decomposing our quasar hosts into bulges and disks, there is a similar $M_{\rm BH}$–$M_{*,\rm bulge}$ relation with slightly larger scatter, likely caused by systematic uncertainties in the bulge–disk decomposition. The $M_{\rm BH}$–$M_{*,\rm host}$ relation at $z_{\rm med} = 0.5$ is similar to that in local quiescent galaxies, with negligible evolution over the redshift range probed by our sample. With direct black hole masses from reverberation mapping and the large dynamical range of the sample, selection biases do not appear to affect our conclusions significantly. Our results, along with other samples in the literature, suggest that the locally measured black hole mass–host stellar mass relation is already in place at $z \sim 1$.

Unified Astronomy Thesaurus concepts: Active galaxies (17); AGN host galaxies (2017); Quasars (1319); Surveys (1671); Black hole physics (159)

Supporting material: figure set

1. Introduction

The observed scaling relations between supermassive black hole (BH) masses and the properties of their host galaxies (e.g., stellar mass and stellar velocity dispersion) in the local universe are the foundation of modern BH–galaxy coevolution models (Magorrian et al. 1998; Ferrarese & Merritt 2000; Gebhardt et al. 2000; Häring & Rix 2004; Gültekin et al. 2009; Kormendy & Ho 2013; McConnell & Ma 2013, and references therein). The tight correlations suggest that active galactic nuclei (AGNs) may play important roles in regulating star formation in the host galaxies via self-regulated BH growth and feedback processes (Silk & Rees 1998; Di Matteo et al. 2005; Heckman & Best 2014). Studying BH scaling relations beyond the local universe is a key to understanding BH and galaxy (co) evolution over cosmic history.

Over the past two decades, various investigations have built an inventory of BH and host measurements to study the redshift evolution of BH–host relations up to $z \sim 3$, including the BH mass–stellar velocity dispersion ($M_{\rm BH}$–σ_*) relation (Treu et al. 2004; Woo et al. 2006, 2010; Shen et al. 2015b; Park et al. 2015; Sexton et al. 2019), the BH mass–bulge/host luminosity ($M_{\rm BH} - L_{*,\rm bulge/host}$) relation (Laor 1998; Peng et al. 2006a, 2006b; Decarli et al. 2010), and the BH mass–bulge/host stellar mass ($M_{\rm BH}$–$M_{*,\rm bulge/host}$) relation (Jahnke et al. 2009; Bennert et al. 2011; Dong & Wu 2016; Suh et al. 2020; Ding et al. 2021), as well as expanding the local baselines to include AGNs of different host properties and lower BH masses (e.g., Greene et al. 2008; Jiang et al. 2011a, 2011b; Reines & Volonteri 2015; Bentz & Manne-Nicholas 2018; Greene et al. 2020; Bennert et al. 2021; Zhao et al. 2021). Some groups found deviations from local scaling relations as a function of z (Peng et al. 2006a, 2006b; Merloni et al. 2010; Woo et al. 2010; Park et al. 2015; Sexton et al. 2019), while others found similar BH–host relations to those in the local universe (e.g., Jahnke et al. 2009; Suh et al. 2020; Li et al. 2021a; Ding et al. 2022; Silverman et al. 2022), which is

also supported by the tight correlation between the sample-averaged BH accretion rate and star formation rate in bulge-dominated galaxies at $z = 0.5$–3 (e.g., Yang et al. 2019).

The measurements of BH mass–host relations can be challenging beyond $z \sim 0.1$ for several reasons. First, direct BH mass measurements based on resolved stellar/gas dynamics are difficult to obtain beyond the local universe, where the BH sphere of influence cannot be readily resolved. Reverberation mapping (RM; Blandford & McKee 1982; Peterson 2014) is the primary method of measuring BH masses for broad-line AGNs (BLAGNs) beyond the local universe, but RM is resource intensive and only available for a small number of objects beyond $z \sim 0.1$ (e.g., Bentz et al. 2013). A secondary BH mass recipe, the single-epoch (SE) virial estimator, is based on the broad-line region (BLR) radius–luminosity (R–L) relation (e.g., Kaspi et al. 2005; Bentz et al. 2013; Du et al. 2016) and can be easily adapted for large samples of BLAGNs at higher redshift. However, Shen & Kelly (2010) demonstrated that there is a statistical bias in SE BH masses for flux-limited samples from the uncertainties in these BH masses. In addition, the applicability of SE masses to the high-redshift and high-luminosity regime is not well understood, primarily because the local RM AGNs used to derive the R–L relation are not representative of the general quasar population (e.g., Shen et al. 2015a; Du & Wang 2019; Fonseca Alvarez et al. 2020), and the extrapolated R–L relations for broad Mg II and C IV used for high-redshift BLAGNs are not as well studied as the local R–L relation based on broad Hβ (Bentz et al. 2013).

Host galaxy properties are also difficult to measure, as the unobscured AGN (where virial BH masses are feasible) usually far outshines the host galaxy. For imaging studies, high-resolution images, such as those from the Hubble Space Telescope (HST), are often necessary to robustly decompose the quasar and host light. However, rigorous image analysis reveals that host galaxies of local AGNs ($z < 0.35$) often consist of complex structures, including spiral arms and tidal and merger features, in addition to the main galaxy components (bars, bulges, and disks) (Kim et al. 2017). These complex structures are extremely challenging to measure even with HST at higher redshifts.

Due to difficulties in obtaining BH mass and host properties, many studies are limited to specific samples that may introduce selection biases. Earlier studies were often restricted to the bright end of BLAGNs and had small sample sizes and limited dynamical ranges in BH/host properties. Lauer et al. (2007) showed that overmassive BHs are favored in flux-limited studies owing to the intrinsic scatter of the scaling relations. For a "bottom-heavy" galaxy luminosity function, there are more low-mass hosts than high-mass ones. However, more massive BHs are preferentially selected in a flux-limited sample based on AGN luminosity, resulting in an average offset in the BH mass–host relations and a shallower slope than the true underlying relation. Schulze & Wisotzki (2011, 2014) argued that additional selection biases could arise from the lack of knowledge in the relevant underlying distribution functions (e.g., the active fraction of AGNs, bulge properties) and their evolution with redshift. These biases can account for a large portion of, if not all, the redshift evolution reported in earlier investigations (Schulze & Wisotzki 2011; Shen et al. 2015b).

In this work, we study the BH scaling relations at $0.2 \lesssim z \lesssim 0.8$ using the Sloan Digital Sky Survey Reverberation Mapping (SDSS-RM; Shen et al. 2015a) sample. The SDSS-RM sample has two major advantages in measuring the redshift evolution of BH–host galaxy relations: (1) the parent sample is a uniformly selected flux-limited BLAGN sample, and thus the selection effects can be quantified and corrected; and (2) BH masses are available from direct RM (Shen et al. 2016; Grier et al. 2017b, 2019; Homayouni et al. 2020), rather than from SE, masses. We have acquired high-resolution imaging for the SDSS-RM sample with HST to measure the host galaxy color and luminosity in two bands, tracing young and old stellar populations, respectively. Our sample includes 38 sources (10 included in a pilot study in Li et al. 2021c), which is comparable in size to the local RM AGN sample used to calibrate the R–L relation (Bentz et al. 2013) and has sufficient statistics and dynamic range in BH mass (and stellar mass) to characterize the redshift evolution of BH scaling relations over the redshift range of $0.2 \lesssim z \lesssim 0.8$.

This paper is organized as follows. We describe our data and analysis in Section 2. The main results are presented in Section 3 and we discuss the biases in the observed BH scaling relations in Section 4. We discuss our results in Section 5 and conclude in Section 6. Throughout this paper we adopt a flat ΛCDM cosmology with $\Omega_M = 0.3$ and $H_0 = 70\,\mathrm{km\,s^{-1}\,Mpc^{-1}}$. All host galaxy measurements refer to the stellar population only.

2. Observation and Data Analysis

2.1. Sample

Our sample consists of 38 SDSS-RM quasars at $0.2 \lesssim z \lesssim 0.8$ (median redshift $z_{\rm med} = 0.5$) with RM-based BH masses; 37 of these RM masses were based on the broad Hβ line (Shen et al. 2016; Grier et al. 2017b), with one source (RM767) based on the broad Mg II line (Shen et al. 2016). Ten sources in our HST sample were studied in a pilot program (Li et al. 2021c); 28 sources are presented in this work for the first time. Among the 44 quasars with Hβ RM BH masses in Grier et al. (2017b), seven sources beyond $z \sim 0.8$ were excluded from the HST programs to ensure more robust host galaxy measurements and to avoid unknown selection biases, as the lag detection fraction at $z \gtrsim 0.8$ is significantly lower than that at lower redshifts (see, e.g., Figure 1). Figure 1 presents the redshift and luminosity distribution of our sample, and Table 1 summarizes the physical properties of these objects.

2.2. Black Hole Masses

RM determines BH masses by measuring the time delay in variability between the continuum and broad emission lines. The time delay corresponds to the light-travel time between the continuum-emitting accretion disk and the BLR. Assuming that the BLR is virialized, a BH mass can be calculated using the time lag (τ) and the width of the broad emission line (ΔV) via the equation

$$M_{\rm BH} = f\frac{c\tau\Delta V^2}{G}, \quad (1)$$

where G is the gravitational constant and f is a dimensionless factor of order unity that accounts for BLR geometry, kinematics, and inclination. The line width ΔV can be estimated from either the FWHM or the line dispersion ($\sigma_{\rm line}$) of the broad line measured from the mean or rms spectra (e.g., Wang et al. 2019).

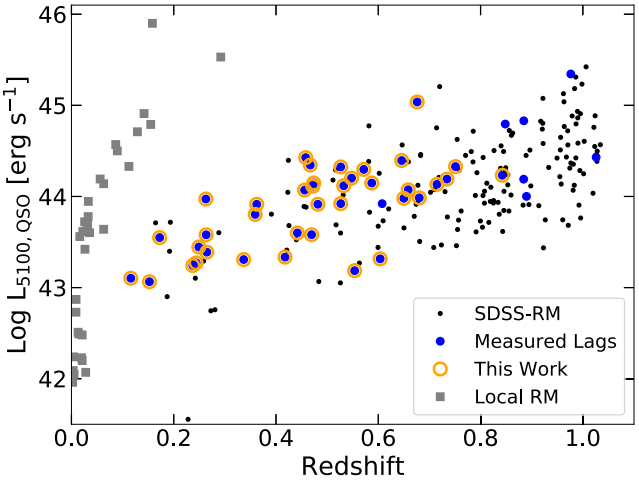

Figure 1. Quasar luminosity and redshift distribution of our sample (open orange circles), and a representative subset of the local RM sample (from Bentz et al. 2013; gray squares). The parent SDSS-RM sample (black circles) and those with measured lags (blue circles) from Grier et al. (2017b) are also labeled for reference.

For the majority of our sources, we adopt the RM BH masses from Grier et al. (2017b) computed using a consant virial coefficient of $f = 4.47$ based on $\sigma_{\rm line}$ measured from the rms spectra (equivalent to $f = 1.12$ when using the FWHM for ΔV). For RM767, Shen et al. (2016) measured a lag between the continuum and broad Mg II line during the first-year monitoring. However, the lag significance is reduced in the more recent analysis in Homayouni et al. (2020) using 4 yr light curves, as the broad Mg II line does not display a strong response to the continuum in the following years. We adopt the Shen et al. (2016) Mg II lag for RM767 and use its $\sigma_{\rm line}$ measured from the rms spectrum to derive a BH mass. For three of our sources, RM316, RM519 and RM767, the original $\sigma_{\rm line}$ measurements in Grier et al. (2017b) and Li et al. (2021c) are significantly overestimated owing to poor line fitting in the spectral analysis. Here we reanalyze the first-year rms spectra with `prepspec` and update the $\sigma_{\rm line}$ and RM BH masses for the three sources.[14] The BH mass uncertainties from Grier et al. (2017b) are calculated by propagating the statistical uncertainties of the lag and line width measurements and then adding a systematic uncertainty of 0.16 dex, which is the scatter estimated from repeated RM measurements in local RM campaigns (Fausnaugh et al. 2017). However, the adopted BH mass uncertainty is still an underestimation, as it does not account for the intrinsic scatter in the virial coefficient for individual systems, which could lead to additional BH mass uncertainties of as large as ~ 0.3 dex (Grier et al. 2017a; Shen et al. 2023). The BH masses are tabulated in Table 1 (with updates from earlier work indicated by an asterisk).

2.3. HST Imaging Analysis

The HST observations for the 28 new objects were conducted between 2019 December 23 and 2021 June 9 in Cycle 27 (GO-15849, PI: Shen). Our observational design is identical to the pilot program (GO-14109, PI: Shen): each target was observed with two dedicated orbits, one in UVIS filters (F606W for $z < 0.6$ and F814W for $z > 0.6$) and one in IR filters (F110W for $z < 0.6$ and F140W for $z > 0.6$), which are chosen to cover similar rest-frame wavelengths at different redshifts. Two additional orbits were used to observe the white dwarf EGGR-26 to construct the point-spread function (PSF) models in all bands used for this program. All observations were performed in dithered patterns (three-point dithering for UVIS filters and four-point dithering for IR filters) to improve PSF sampling. The data were processed using standard HST calibration procedures and geometrically corrected and dither-combined with *astrodrizzle*. The final image sampling is $0\farcs033$ pixel^{-1} for the UVIS F606W/F814W images and $0\farcs066$ pixel^{-1} for the IR F110W/F140W images, which correspond to $\sim$0.2 and $\sim$0.4 kpc at $z = 0.5$, respectively. The FWHM of the PSF is $\sim$2.2 pixels for the IR images and $\sim$1.8 pixels for the UVIS images.

For RM177, our HST program only covers the IR band because this object was observed in UVIS (F606W and F814W) from a previous HST program (GO-10134; PI: Davis; Davis et al. 2007). We processed the individual UVIS exposures from this earlier program following the same procedures for our HST program, and the final imaging sampling is $0\farcs05$ pixel^{-1} ($\sim$0.3 kpc at $z = 0.5$). We use a field star in the same field of view as the PSF model for the UVIS images of RM177.

We then follow the procedures in Li et al. (2021c) and perform 2D image decomposition to separate the quasar and host light using `GALFIT` (Peng et al. 2010), but with two modifications. First, we allow each system to be fitted by a PSF +disk model (Sérsic index $n = 1$), in addition to the PSF +bulge model ($n = 4$) and PSF+bulge+disk model. Upon our analysis with the full sample, we identified several sources whose hosts are best fitted by an exponential disk, rather than a bulge or bulge+disk model as used in Li et al. (2021c). Second, we revise our model-selection criteria using reduced χ^2 calculated from a small region surrounding the target. By default, `GALFIT`'s reduced χ^2 is calculated from the entire image analysis area (e.g., roughly $10'' \times 10''$), where >60% of all the pixels are background, so the reduced χ^2 can change based on the chosen image size and is largely determined by the accuracy of the background estimation. To assess the quality of the fit, we calculate $r\chi^2_e$, the reduced χ^2 within the best-fit ellipse at 3σ sky background (estimated by `GALFIT`) around the source. If $\Delta(r\chi^2_e) > 5$ (threshold chosen by visual inspection of the data) between the PSF+bulge+disk model and the two-component models (PSF+bulge or PSF+disk), we consider there to be strong evidence that the additional component is necessary and adopt the three-component model; otherwise, we select the two-component model (PSF+bulge or PSF+disk) with the smaller $r\chi^2_e$ as the best-fit model.

To briefly summarize our fitting procedure, we first fit the IR images with three different models: PSF+bulge (Sérsic index $n = 4$), PSF+disk ($n = 1$), and PSF+bulge+disk. The fit is considered successful when the best-fit parameters are within reasonable ranges (i.e., the effective radius of the Sérsic component $R_e > 1$ pixel, axis ratio $q > 0.01$), which is to prevent introducing additional components fitting for mismatched PSF or other small-scale features. While the galaxy may not be a perfect bulge or disk, Kim et al. (2008) showed

[14] Details of the final SDSS-RM spectra analysis and lag results are described in Shen et al. (2023). However, the lag methodology and detection criteria in Shen et al. (2023) are optimized for the entire SDSS-RM sample and the longer multiyear light curves, so we adopt the lag results from the earlier papers, which are optimized for the first-year light curves and shorter lags. Our results and conclusions remain the same if we adopt the RM BH masses from Shen et al. (2023).

Table 1
Target Properties

RMID	R.A. (J2000) (deg)	Decl. (J2000) (deg)	z	i_{psf} (mag)	$L_{5100,\ QSO}$ (erg s^{-1})	$\log(M_{BH,\ SE})$ ($M_\odot$)	$\log(M_{BH,\ RM})$ ($M_\odot$)
017	213.3511	53.0908	0.4559	19.21	43.9	8.36 ± 0.04	$8.92^{+0.24}_{-0.19}$
033	213.8848	52.8183	0.7147	20.49	44.1	7.60 ± 0.03	$7.23^{+0.23}_{-0.20}$
101	213.0592	53.4296	0.4581	18.84	44.4	7.89 ± 0.004	$7.26^{+0.17}_{-0.19}$
160	212.6719	53.3136	0.3593	19.68	43.8	8.20 ± 0.007	$7.85^{+0.18}_{-0.17}$
177	214.3525	52.5069	0.4818	19.56	44.0	8.43 ± 0.03	$7.57^{+0.55}_{-0.20}$
191	214.1899	53.7463	0.4418	20.45	43.6	7.55 ± 0.01	$6.90^{+0.22}_{-0.16}$
229	212.5752	53.4937	0.4696	20.27	43.6	8.00 ± 0.07	$7.65^{+0.17}_{-0.20}$
265	215.0995	53.2681	0.7343	20.65	44.2	8.31 ± 0.02	$8.58^{+0.23}_{-0.26}$
267	212.8030	53.7520	0.5872	19.62	44.1	7.92 ± 0.02	$7.41^{+0.17}_{-0.17}$
272	214.1071	53.9107	0.2628	18.82	43.9	7.82 ± 0.02	$7.58^{+0.18}_{-0.21}$
300	214.9213	53.6138	0.6457	19.49	44.5	8.19 ± 0.02	$7.60^{+0.17}_{-0.20}$
301	215.0427	52.6749	0.5477	19.76	44.1	8.53 ± 0.09	$8.64^{+0.25}_{-0.22}$
305	212.5178	52.5281	0.5266	19.50	44.2	7.92 ± 0.01	$8.32^{+0.16}_{-0.16}$
316	215.2185	52.9396	0.6760	18.03	45.0	8.50 ± 0.006	$^{*}7.55^{+0.17}_{-0.17}$
320	215.1605	53.4046	0.2647	19.47	43.4	8.06 ± 0.02	$7.67^{+0.18}_{-0.18}$
338	214.9818	53.6687	0.4177	20.08	43.4	8.36 ± 0.05	$7.69^{+0.27}_{-0.24}$
371	212.8476	52.2255	0.4719	19.57	44.1	8.13 ± 0.02	$7.38^{+0.16}_{-0.16}$
377	215.1814	52.6032	0.3368	19.77	43.4	7.90 ± 0.03	$7.20^{+0.16}_{-0.16}$
392	215.3012	52.6965	0.8425	20.44	44.3	8.19 ± 0.04	$8.22^{+0.19}_{-0.18}$
457	213.5714	51.9563	0.6037	20.29	43.4	8.10 ± 0.1	$8.03^{+0.18}_{-0.21}$
519	214.3012	51.9460	0.5538	21.54	43.2	7.36 ± 0.08	$^{*}7.38^{+0.18}_{-0.19}$
551	212.9461	51.9388	0.6802	21.52	44.0	7.66 ± 0.03	$6.95^{+0.19}_{-0.19}$
589	215.2053	52.1815	0.7510	20.74	44.4	8.52 ± 0.02	$9.00^{+0.18}_{-0.18}$
601	212.2685	54.0623	0.6585	20.10	44.1	9.06 ± 0.05	$8.45^{+0.36}_{-0.24}$
622	212.8133	51.8692	0.5716	19.55	44.3	8.22 ± 0.08	$7.94^{+0.19}_{-0.16}$
634	212.8995	51.8346	0.6500	20.76	44.0	7.46 ± 0.03	$7.56^{+0.27}_{-0.24}$
645	215.1658	52.0666	0.4738	19.78	44.1	8.22 ± 0.01	$7.57^{+0.16}_{-0.18}$
694	214.2778	51.7278	0.5324	19.62	44.2	7.59 ± 0.008	$6.70^{+0.35}_{-0.17}$
720	211.3251	53.2583	0.4670	19.03	44.3	8.14 ± 0.007	$7.74^{+0.22}_{-0.18}$
767	214.2122	53.8658	0.5266	20.23	43.9	7.51 ± 0.04	$^{*}7.63^{+0.17}_{-0.16}$
772	215.3996	52.5275	0.2491	18.87	43.4	7.63 ± 0.02	$6.60^{+0.22}_{-0.22}$
775	211.9961	53.7999	0.1725	17.91	43.5	7.93 ± 0.008	$7.67^{+0.39}_{-0.24}$
776	212.0504	53.8842	0.1161	17.98	43.1	7.80 ± 0.007	$7.26^{+0.17}_{-0.19}$
779	214.8474	54.3671	0.1525	19.10	43.1	7.43 ± 0.01	$7.18^{+0.17}_{-0.17}$
781	215.2647	51.9721	0.2634	19.31	43.6	7.77 ± 0.01	$7.89^{+0.16}_{-0.16}$
782	213.3290	54.5340	0.3623	18.89	43.9	8.01 ± 0.009	$7.51^{+0.16}_{-0.18}$
790	214.3720	53.3074	0.2374	18.67	43.3	8.43 ± 0.01	$8.28^{+0.48}_{-0.23}$
840	214.1881	54.4280	0.2439	18.63	43.2	8.29 ± 0.03	$7.93^{+0.21}_{-0.20}$

Note. RM BH masses are based on Hβ lags from Grier et al. (2017b), except for RM767, which is based on the Mg II lag from Shen et al. (2016). The quasar luminosities and the SE BH masses are from Shen et al. (2015b). $L_{5100,QSO}$ is the host-light-subtracted quasar continuum luminosity at rest frame 5100 Å. The SE BH mass uncertainties are 1σ measurement errors only, but SE BH masses are typically dominated by a systematic uncertainty of ∼0.5 dex. The RM BH mass uncertainties also include 0.16 dex systematic uncertainty following Grier et al. (2017b). M_{BH} for RM316, RM519, and RM767 (labeled with asterisks) are updated from Grier et al. (2017b) and Li et al. (2021c) as described in Section 2.2.

that fixing the Sérsic index results in more accurate flux recovery during host decomposition when the host galaxy is faint. We use $\Delta(r\chi^2_e)$ to select the best-fit model from the successful PSF+bulge, PSF+disk, and PSF+bulge+disk models. In addition to the quasar+host, we fit additional PSF and/or Sérsic models for nearby objects to ensure that the host decomposition and sky background estimation are not strongly affected by nearby objects (see, e.g., RM033, RM101, RM694, and RM776).

We visually inspect all the GALFIT images and manually adjust the GALFIT models only when necessary. Upon visual inspection, the background in RM776 is high owing to a nearby bright object, and adding another component improves the fitting of its surface brightness profile significantly, so we adopt a three-component model for RM776. RM775 and RM790 display extended truncated ring features in the residual images of the PSF+bulge+disk model, so a fourth component (an inner-truncated disk) was added to ensure robust flux recovery for the host. The truncated disk in RM775 is also fitted with Fourier modes to account for the irregular ellipsoid shape. However, we only include the main disk component in the PSF+bulge+disk model, and not the truncated disk, for estimating the final photometry for the disks. Finally, we fit the flux of each component in the UVIS images by fixing the shape

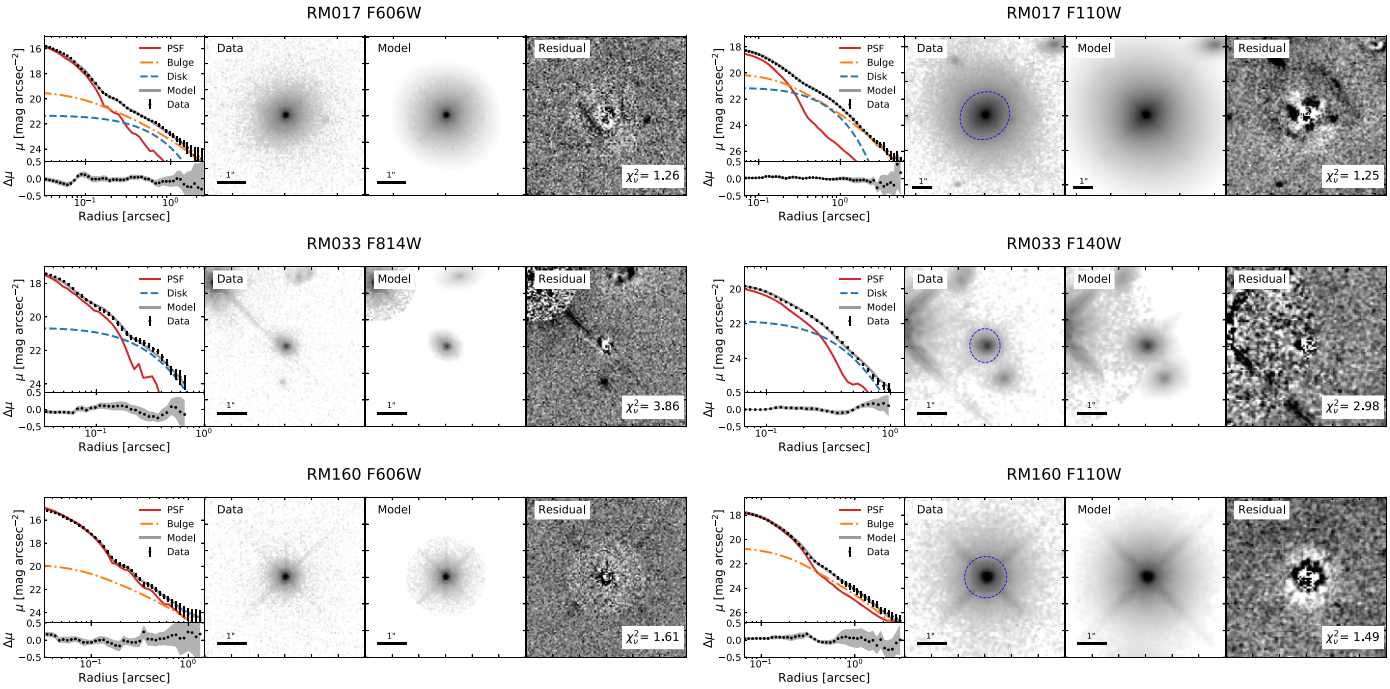

Figure 2. Examples of surface brightness decomposition of three quasars with GALFIT; from top to bottom are sources that are best fitted by a PSF+bulge+disk, PSF +disk, and PSF+bulge model, respectively. The left panels are the surface brightness profiles of the data (black circles), the model (gray solid line), and each modeled component (red solid lines for PSFs, orange dotted–dashed lines for bulges ($n = 4$), blue dashed lines for exponential disks ($n = 1$), and purple dotted lines for truncated rings (RM775 and RM790)). The radial profiles are directly measured from the GALFIT decomposed models and the HST images with isophote fitting. The leftmost bottom subpanel for each object is the residual of the surface brightness profile, with the rms along the isophote elliptical plotted in gray. The three images on the right are (from left to right) the HST image, the GALFIT model, and the residual. The blue ellipse in the HST image (IR only) encloses the area above 3σ sky background in the best-fitting model. The residual images display the 1st–99th percentiles (with linear stretch) of the residual values to provide better visual contrast. The reduced χ^2 of the model is labeled in the lower right corner of each residual image. The full figure set is available online.

(The complete figure set (77 images) is available.)

and structural parameters (Sérsic index, effective radius, ellipticity, and position angle) to the best-fit model in the IR images. For the sources that preferred the three-component model in the IR image, we check whether the three components in the UVIS image converge on similar relative positions to those in the IR image, which ensures that the model is fitting the same physical structures in the two bands. The bulge and disk components of two sources, RM267 and RM316, failed to converge at similar central positions, so the two-component model (PSF+bulge) is adopted instead. Figure 2 presents a few examples of our GALFIT decomposition, and the GALFIT decomposition results are tabulated in Table 2. The complete figure set, data, PSF templates, and GALFIT decomposition models are available via ftp://quasar.astro.illinois.edu/public/sdssrm/paper_data/Li_2023_HST_host.

During our analysis of the full HST sample, we discovered an error in our GALFIT analysis in the pilot study (Li et al. 2021c). The ncombine parameter was input incorrectly, which caused the sigma image produced by GALFIT to be overestimated by a factor of ~ 4 in areas dominated by emission (see GALFIT user manual, Equation (33)). The error mainly affects the estimation of χ^2 but does not change the fitting results, i.e., all fitted parameters are consistent with the results with the correct sigma images within the uncertainties. We include updated measurements for the 10 objects in the pilot study in Table 2.

GALFIT only accounts for statistical uncertainties between the data and the model and does not take into account PSF mismatches or complex spatial structures. There are three major sources of flux uncertainties: (1) the temporal variability of the HST PSF (derived from the difference between the dedicated PSF observation and field stars in science observations, $\sim$0.07 mag in UVIS and $\sim$0.03 mag in IR), (2) the deviation between the GALFIT model and the image ($\sim$0.02 mag in UVIS and $\sim$0.005 mag in IR), and (3) fixing the Sérsic index ($\sim$0.05 mag for PSF and $\sim$0.2 mag for the host/bulge/disk). We combine these flux uncertainties and adopt typical values of 0.1 and 0.25 mag as the final uncertainties for the PSF and galaxy (bulge, disk, or galaxy) flux measurements in all bands, respectively. These final uncertainties are consistent with those in our pilot study and similar observations and simulations in the literature (e.g., Kim et al. 2008; Jahnke et al. 2009; Park et al. 2015; Bentz & Manne-Nicholas 2018). See Li et al. (2021c) for additional technical details on the flux uncertainty budget.

2.4. Host Galaxy/Bulge Masses

Following the approach in Li et al. (2021c), we convert the UVIS/IR photometry to rest-frame B and I/R band and estimate the host/bulge stellar masses with the color–M_*/L relations (CMLRs) from Into & Portinari (2013) and CIGALE (Boquien et al. 2019). First, we correct for Galactic extinction using the recalibrated Schlegel et al. (1998) dust map and reddening from Schlafly & Finkbeiner (2011). We then fit the extinction-corrected HST photometry with CIGALE to derive k-corrections and color transformations between the HST filters and the Johnson–Cousins filters. CIGALE is a spectral energy distribution (SED) fitting code

Table 2
Galaxy Decomposition Results

RMID	Comp.	mag_{UVIS}	mag_{IR}	r (arcsec)	n	q	P.A.	$r\chi^2_{UVIS}$	$r\chi^2_{IR}$
017	PSF	20.15	21.19					1.26	1.25
	Bulge	19.98	19.88	1.50	4	0.89	149.0		
	Disk	21.58	21.11	0.63	1	0.67	53.2		
033	PSF	21.69	22.59					3.86	2.98
	Disk	22.36	23.01	0.27	1	0.69	−60.0		
101	PSF	19.41	20.53					1.43	1.17
	Bulge	21.17	21.14	0.71	4	0.88	−158.4		
160	PSF	19.35	20.52					1.61	1.49
	Bulge	21.28	21.27	0.67	4	0.99	79.0		
177	PSF	20.06	21.60					1.76	1.37
	Disk	21.53	21.53	0.53	1	0.50	151.3		
191	PSF	23.02	24.29					1.28	2.12
	Bulge	23.22	22.26	0.50	4	0.17	−130.1		
	Disk	20.81	20.91	1.33	1	0.54	−154.5		
229	PSF	21.49	22.49					1.24	1.89
	Bulge	24.70	23.22	0.31	4	0.21	−118.5		
	Disk	21.66	21.61	0.78	1	0.69	−134.4		
265	PSF	21.57	22.55					1.24	1.36
	Disk	20.84	21.01	1.36	1	0.95	118.9		
267	PSF	20.25	21.64					1.36	1.70
	Bulge	21.11	21.12	0.37	4	0.71	67.1		
272	PSF	19.10	20.31					1.26	1.62
	Bulge	21.47	21.47	0.31	4	0.56	144.0		
	Disk	21.01	21.43	0.82	1	0.34	123.0		
300	PSF	20.39	21.56					1.36	2.32
	Disk	21.75	22.33	0.40	1	0.97	−123.1		
301	PSF	21.02	22.42					1.32	1.64
	Bulge	22.58	21.66	0.32	4	0.34	37.0		
	Disk	21.37	21.38	1.44	1	0.69	47.4		
305	PSF	20.39	21.31					1.48	1.39
	Bulge	21.17	20.90	0.68	4	0.88	71.6		
316	PSF	19.07	20.35					1.41	2.38
	Bulge	20.88	21.10	0.96	4	0.68	27.4		
320	PSF	20.75	21.81					1.27	2.73
	Bulge	21.80	21.65	0.21	4	0.66	−138.5		
	Disk	19.88	20.02	2.41	1	0.34	154.5		
338	PSF	21.14	21.96					1.39	1.47
	Disk	20.94	21.18	0.68	1	0.89	−50.5		
371	PSF	20.29	21.21					1.35	2.09
	Bulge	20.88	20.77	1.11	4	0.86	45.0		
377	PSF	22.64	23.32					1.15	1.59
	Bulge	21.06	20.91	0.33	4	0.52	100.8		
	Disk	21.36	21.52	1.12	1	0.92	−174.1		
392	PSF	22.62	23.18					1.29	1.42
	Bulge	21.94	22.10	0.60	4	0.71	151.6		
457	PSF	22.71	23.56					1.20	1.31
	Bulge	22.43	22.21	0.78	4	0.75	139.4		
519	PSF	22.76	23.59					1.19	1.37
	Bulge	23.55	23.51	0.15	4	0.63	−126.1		
551	PSF	22.37	23.71					1.29	1.28
	Bulge	22.34	22.53	0.15	4	0.70	42.2		

Table 2
(Continued)

RMID	Comp.	mag_{UVIS}	mag_{IR}	r (arcsec)	n	q	P.A.	$r\chi^2_{UVIS}$	$r\chi^2_{IR}$
589	PSF	21.50	22.33					1.29	1.63
	Disk	22.19	22.20	0.55	1	0.47	31.6		
601	PSF	21.33	22.20					1.29	1.62
	Disk	21.38	21.46	1.02	1	0.58	56.2		
622	PSF	20.55	21.59					6.73	1.12
	Bulge	21.65	21.24	0.50	4	0.70	118.1		
634	PSF	21.85	22.68					1.32	1.50
	Disk	22.17	22.38	0.76	1	0.34	118.6		
645	PSF	20.47	21.36					1.41	1.74
	Bulge	21.23	21.46	0.31	4	0.89	77.7		
694	PSF	20.41	21.57					1.20	1.63
	Bulge	23.07	23.85	0.78	4	0.76	−144.2		
720	PSF	20.27	21.24					1.40	2.52
	Bulge	20.69	21.14	0.37	4	0.87	50.3		
767	PSF	21.59	22.20					1.18	1.31
	Bulge	21.16	21.26	1.48	4	0.73	169.0		
772	PSF	21.78	22.40					1.17	1.00
	Bulge	18.69	18.99	1.58	4	0.88	88.8		
775	PSF	19.73	21.02					1.19	2.14
	Bulge	19.58	19.69	0.18	4	0.71	−175.7		
	Disk	18.87	19.03	2.32	1	0.78	139.7		
	UVIS Trunc.	21.83		0.42	1	0.6	156.0		
	Fourier		−0.56	0.14	0.10	−0.07	0.04		
	Fourier		4.35	2.58	32.19	19.36	1.16		
	Radial			0.33	1.08	0.40	152.5		
	Fourier		0.53	0.33	0.17	0.04	0.02		
	Fourier		−161.59	4.08	−43.21	−3.69	−2.25		
	IR Trunc.		23.89	0.24	1	0.52	139.2		
	Fourier		−0.53	0.08	0.06	−0.02	0.05		
	Fourier		47.96	10.96	41.73	18.83	14.42		
	Radial			0.88	1.38	0.52	136.5		
	Fourier		0.56	0.11	−0.07	−0.03	−0.07		
	Fourier		−125.58	12.36	5.47	0.66	−16.27		
776	PSF	20.34	21.40					0.43	0.09
	Bulge	19.33	19.32	0.46	4	0.77	176.8		
	Disk	19.33	19.49	2.17	1	0.35	−156.8		
779	PSF	20.19	20.98					1.32	1.19
	Disk	20.38	20.84	0.75	1	0.57	−35.5		
781	PSF	20.53	21.81					1.33	1.80
	Bulge	20.84	20.87	0.33	4	0.45	68.4		
	Disk	20.86	21.27	1.01	1	0.71	−156.6		
782	PSF	19.83	21.18					1.38	2.10
	Bulge	22.52	22.16	0.52	4	0.28	48.2		
	Disk	20.21	20.32	1.63	1	0.72	−0.8		
790	PSF	21.29	21.92					1.30	2.06
	Bulge	19.70	19.79	0.53	4	0.75	122.1		
	Disk	21.48	20.95	0.47	1	0.64	35.5		
	UVIS Trunc.	25.47		0.71	1	0.50	121.7		
	Radial			2.60	4.43	0.52	122.4		
	IR Trunc.		25.22	0.91	1	0.49	122.1		
	Radial			2.58	4.10	0.54	123.3		
840	PSF	20.45	22.37					1.30	2.67

Table 2
(Continued)

RMID	Comp.	mag_{UVIS}	mag_{IR}	r (arcsec)	n	q	P.A.	$r\chi^2_{UVIS}$	$r\chi^2_{IR}$
	Bulge	20.19	19.98	0.26	4	0.86	36.1		
	Disk	19.82	19.97	2.95	1	0.23	56.1		

Note. Here r is the effective radius of the Sérsic component, n is the Sérsic index, q is the ratio between the semiminor axis and the semimajor axis, and P.A. is the position angle at the semimajor axis in degrees. The reduced χ^2 is calculated from the image residual, as reported by GALFIT. Magnitudes are reported in ST magnitude ($mag_{ST} = -2.5\log(F_\lambda[\mathrm{erg\ s^{-1}\ cm^{-2}\ \AA^{-1}}]) - 21.1$) , which is the default output from GALFIT. For RM775 and RM790, we include the best-fit parameters for the truncated disks in the UVIS and IR images: the magnitudes are the surface brightness at the break radius (mag $\mathrm{arcsec^{-2}}$), and the best-fit parameters for the truncated radial profiles are listed in the order of the 1% flux radius (softening length, in arcseconds), 99% flux radius (break radius, in arcseconds), q, and P.A. The truncated disk in RM775 is fitted with Fourier modes in both the disks and truncated radial profiles, and the best-fit Fourier amplitudes (first row) and phase angles (second row) are listed in the order of Fourier mode 1, 3, 4, 5, 6. No extinction corrections are made for these magnitudes. The uncertainties of the GALFIT results are discussed in Section 2.

that can model galaxy and AGN emission from multiwavelength photometry. We set up a simple CIGALE model that includes basic stellar population synthesis models (Maraston 2005), an initial mass function (Kroupa 2001), a dust attenuation model (Calzetti et al. 2000; Leitherer et al. 2002), and a delayed star formation history with optional starburst. We do not include the AGN model for modeling the quasar-subtracted photometry. The UVIS filters are converted to *B*-band magnitudes, and the IR filters are converted to *I*-band and *R*-band filters depending on the source redshift (F110W to *I* band at $z < 0.4$ and *R* band $z > 0.4$; F140W to *I* band at $z < 0.7$ and *R* band at $z > 0.7$).

We estimate the host and bulge stellar masses with the CMLR for dusty galaxy models from Into & Portinari (2013) using the rest-frame photometry and their uncertainties. CIGALE fits provide the *k*-corrected photometry, from which we estimate stellar mass with the CMLR relation, and a stellar mass from the best-fit SED model. For RM177 (with two UVIS bands from a separate HST program), we include both the F606W and F814W bands for the CIGALE fitting but only use the F606W band (rest-frame *R* band) for the CMLR stellar mass estimation. The CMLR stellar mass uncertainties are propagated directly from the photometry uncertainties, and the CIGALE stellar mass uncertainties are estimated from the SED modeling. Both CMLR and CIGALE uncertainties are consistently around 0.3 dex, which is typical for stellar mass estimation from two-band photometry.

The final Galactic-extinction-corrected, *k*-corrected, band-converted magnitudes and the host/bulge stellar masses are tabulated in Table 3. We adopt the CMLR stellar masses as our nominal host/bulge stellar masses. The best-fit stellar masses from CIGALE are also reported for comparison, which are systematically smaller than the CMLR masses by ~0.08 dex but still consistent within uncertainties. The only exception is RM265. The color derived for RM265 from CIGALE is unusually red, which led to a large, likely unphysical, host stellar mass ($>10^{12}\ M_\odot$) using the CMLR. However, the typical *B*–*R* color is roughly $0.3 < (B - R) < 1.3$, derived from all galaxy types in the Kinney–Calzetti Spectral Atlas (Calzetti et al. 1994; Kinney et al. 1996). If we assume a red color of 1.3 and adopt the *R*-band luminosity for the CMLR, the host stellar mass for RM265 is $\log(M_*) = 11.23$, which is consistent with the stellar mass derived from CIGALE. We show both the CMLR and CIGALE masses for RM265 in the figures and use the more physical CIGALE mass (for RM265 only) when fitting the BH scaling relations and their redshift evolution in our analysis.

3. Results

3.1. Host Properties

At $z > 0.2$, it becomes challenging to perform bulge/disk decomposition owing to limited spatial resolution, even with HST. Our GALFIT analysis shows that 16 (out of 38) quasars are best fitted by the PSF+bulge model, 9 quasars are best fitted by the PSF+disk model, and 13 quasars are decomposed into PSF+bulge+disk models. In addition, 26 hosts are bulge dominated, i.e., $M_{*,\ \mathrm{bulge}} > M_{*,\ \mathrm{disk}}$, and 12 hosts are disk dominated. A best-fit profile of $n = 4$ ($n = 1$) in our analysis does not necessarily mean that the host galaxy is an elliptical (spiral) galaxy; the Sérsic index is fixed to $n = 1$ or $n = 4$ to ensure that the quasar/host decomposition is robust and not to provide rigorous classifications of host morphology. In fact, a majority of local elliptical galaxies are not well described by single Sérsic components (e.g., Huang et al. 2013), and exponential profiles do not always indicate the presence of disks.

The structural parameters (ellipticity, Sérsic index, effective radius) of the bulge/disk-dominated sources in our sample are broadly consistent with the statistical distributions from ~2500, *i*-mag <22 SDSS quasar hosts observed by the Hyper Suprime-Cam (HSC) on the Subaru telescope (Li et al. 2021b). When we allow the Sérsic index to vary in the GALFIT fitting, the median (minimum, maximum) Sérsic index of our two-component model is 2.0 (0.6/7.0), similar to the distribution in Li et al. (2021b). There are more disk-like ($n < 2$) hosts in the SDSS-HSC sample but roughly equal numbers of bulge-like and disk-like hosts (Sérsic indices above and below 2) in our sample. The size and ellipticity of our quasar hosts are also similar to the SDSS-HSC sample. The median (16th and 84th percentiles) effective radius is $0\farcs68$ ($0\farcs35/0\farcs92$), and the median (16th/84th percentiles) ellipticity ($1 - q$) is 0.28 (0.11/0.41) for our sample.

We also examine the offset between the quasar position and the host centroid in the IR images, where the centroid of the host galaxy is better constrained than in the UVIS band. Off-centered AGN/quasars may indicate ongoing galaxy mergers or recoiling SMBHs from binary SMBH coalescence (Loeb 2007; Comerford & Greene 2014). Figure 3 shows that most (34/38) of the quasars are located within <1 kpc of the host galaxy center. The four sources with significant offsets (> 1 kpc, RM265, RM267, RM634, RM645; see the images and GALFIT models in the full Figure 2 figure set online) show signs of galaxy interaction or mergers, which would complicate

Table 3
Final Photometry, Color, Luminosity, and Stellar Mass

RMID	Bands	Comp	m_B (mag)	$m_{I/R}$ (mag)	Color (mag)	$\log L_{\rm B}$ ($L_\odot$)	$\log L_{\rm I/R}$ ($L_\odot$)	$\log M_*$ ($M_\odot$)	$\log M_{*,\rm CIGALE}$ ($M_\odot$)
017	*B, R*	Host	19.66	18.78	0.88	11.49 ± 0.10	11.07 ± 0.10	11.06 ± 0.35	10.91 ± 0.31
		Bulge	19.86	19.03	0.84	11.40 ± 0.10	10.98 ± 0.10	10.92 ± 0.35	10.77 ± 0.31
		Disk	21.43	20.36	1.06	10.86 ± 0.10	10.44 ± 0.10	10.60 ± 0.35	10.36 ± 0.32
033	*B, R*	Disk	22.13	21.79	0.34	10.76 ± 0.10	10.34 ± 0.10	9.83 ± 0.35	9.88 ± 0.28
101	*B, R*	Bulge	21.05	20.24	0.81	10.92 ± 0.10	10.50 ± 0.10	10.42 ± 0.35	10.25 ± 0.30
160	*B, I*	Bulge	21.36	20.16	1.20	10.70 ± 0.10	10.15 ± 0.10	9.94 ± 0.27	9.95 ± 0.30
177	*B, R*	Disk	20.86	20.38	0.48	10.91 ± 0.10	10.49 ± 0.10	10.11 ± 0.35	9.78 ± 0.46
191	*B, R*	Host	20.61	19.76	0.85	11.07 ± 0.10	10.65 ± 0.10	10.61 ± 0.35	10.43 ± 0.30
		Bulge	23.09	21.63	1.46	10.32 ± 0.10	9.90 ± 0.10	10.43 ± 0.35	10.00 ± 0.36
		Disk	20.79	20.02	0.77	10.97 ± 0.10	10.55 ± 0.10	10.43 ± 0.35	10.28 ± 0.30
229	*B, R*	Host	21.44	20.55	0.90	10.82 ± 0.10	10.40 ± 0.10	10.41 ± 0.35	10.23 ± 0.31
		Bulge	24.40	22.67	1.73	9.97 ± 0.10	9.55 ± 0.10	10.33 ± 0.35	9.85 ± 0.38
		Disk	21.58	20.77	0.81	10.73 ± 0.10	10.31 ± 0.10	10.24 ± 0.35	10.10 ± 0.31
265	*B, R*	Disk	22.84	20.60	2.23	11.27 ± 0.10	10.85 ± 0.10	12.10 ± 0.35	11.39 ± 0.46
267	*B, R*	Bulge	20.81	20.14	0.67	11.22 ± 0.10	10.80 ± 0.10	10.59 ± 0.35	10.49 ± 0.31
272	*B, I*	Host	20.63	19.58	1.05	10.62 ± 0.10	10.07 ± 0.10	9.76 ± 0.27	9.81 ± 0.29
		Bulge	21.67	20.38	1.29	10.30 ± 0.10	9.75 ± 0.10	9.60 ± 0.27	9.55 ± 0.30
		Disk	21.14	20.28	0.86	10.34 ± 0.10	9.79 ± 0.10	9.34 ± 0.27	9.47 ± 0.29
300	*B, I*	Disk	21.55	20.93	0.61	11.00 ± 0.10	10.45 ± 0.10	9.83 ± 0.27	10.06 ± 0.28
301	*B, R*	Host	20.72	19.82	0.89	11.27 ± 0.10	10.85 ± 0.10	10.85 ± 0.35	10.66 ± 0.31
		Bulge	22.19	20.91	1.28	10.84 ± 0.10	10.42 ± 0.10	10.78 ± 0.35	10.44 ± 0.35
		Disk	21.21	20.47	0.74	11.01 ± 0.10	10.59 ± 0.10	10.44 ± 0.35	10.32 ± 0.31
305	*B, R*	Bulge	20.88	20.01	0.87	11.16 ± 0.10	10.73 ± 0.10	10.72 ± 0.35	10.55 ± 0.31
316	*B, I*	Bulge	20.12	19.68	0.44	11.55 ± 0.10	11.00 ± 0.10	10.25 ± 0.27	10.57 ± 0.26
320	*B, I*	Host	19.91	18.70	1.21	10.98 ± 0.10	10.43 ± 0.10	10.23 ± 0.27	10.21 ± 0.30
		Bulge	22.01	20.61	1.40	10.21 ± 0.10	9.66 ± 0.10	9.60 ± 0.27	9.52 ± 0.30
		Disk	20.06	18.90	1.16	10.90 ± 0.10	10.34 ± 0.10	10.11 ± 0.27	10.11 ± 0.29
338	*B, R*	Disk	20.89	20.27	0.62	10.81 ± 0.10	10.39 ± 0.10	10.14 ± 0.35	10.07 ± 0.30
371	*B, R*	Bulge	20.70	19.87	0.83	11.09 ± 0.10	10.67 ± 0.10	10.62 ± 0.35	10.45 ± 0.31
377	*B, I*	Host	20.54	19.24	1.30	11.00 ± 0.10	10.45 ± 0.10	10.32 ± 0.27	10.23 ± 0.30
		Bulge	21.16	19.80	1.36	10.78 ± 0.10	10.23 ± 0.10	10.14 ± 0.27	10.06 ± 0.30
		Disk	21.45	20.37	1.08	10.55 ± 0.10	10.00 ± 0.10	9.71 ± 0.27	9.74 ± 0.30
392	*B, R*	Bulge	21.76	20.98	0.77	11.26 ± 0.10	10.84 ± 0.10	10.73 ± 0.35	10.58 ± 0.32
457	*B, R*	Bulge	22.04	20.89	1.15	10.94 ± 0.10	10.39 ± 0.10	10.15 ± 0.27	10.15 ± 0.31
519	*B, R*	Bulge	23.30	22.57	0.73	10.18 ± 0.10	9.76 ± 0.10	9.61 ± 0.35	9.50 ± 0.31
551	*B, I*	Bulge	22.20	21.12	1.08	10.98 ± 0.10	10.43 ± 0.10	10.14 ± 0.27	10.14 ± 0.31
589	*B, R*	Disk	22.05	21.13	0.92	11.08 ± 0.10	10.66 ± 0.10	10.69 ± 0.35	10.44 ± 0.32
601	*B, I*	Disk	21.15	20.07	1.07	11.36 ± 0.10	10.81 ± 0.10	10.52 ± 0.27	10.52 ± 0.31
622	*B, R*	Bulge	21.25	20.33	0.91	11.11 ± 0.10	10.69 ± 0.10	10.71 ± 0.35	10.54 ± 0.31
634	*B, I*	Disk	21.81	20.97	0.84	10.99 ± 0.10	10.44 ± 0.10	9.98 ± 0.27	10.09 ± 0.30
645	*B, R*	Bulge	21.14	20.52	0.62	10.84 ± 0.10	10.42 ± 0.10	10.16 ± 0.35	10.08 ± 0.30
694	*B, R*	Bulge	23.10	22.81	0.29	10.05 ± 0.10	9.63 ± 0.10	9.07 ± 0.35	9.10 ± 0.25
720	*B, R*	Bulge	20.62	20.14	0.48	10.97 ± 0.10	10.55 ± 0.10	10.17 ± 0.35	10.14 ± 0.29
767	*B, R*	Bulge	21.02	20.32	0.71	11.03 ± 0.10	10.61 ± 0.10	10.44 ± 0.35	10.31 ± 0.31
772	*B, I*	Bulge	18.88	17.84	1.04	11.26 ± 0.10	10.71 ± 0.10	10.39 ± 0.27	10.42 ± 0.29
775	*B, I*	Host	18.72	17.46	1.25	11.05 ± 0.10	10.50 ± 0.10	10.34 ± 0.27	10.27 ± 0.29
		Bulge	19.84	18.64	1.20	10.58 ± 0.10	10.03 ± 0.10	9.83 ± 0.27	9.82 ± 0.29
		Disk	19.10	17.97	1.13	10.85 ± 0.10	10.30 ± 0.10	10.04 ± 0.27	10.08 ± 0.29
776	*B, I*	Host	18.93	17.62	1.31	10.61 ± 0.10	10.06 ± 0.10	9.94 ± 0.27	9.87 ± 0.30
		Bulge	19.73	18.31	1.41	10.34 ± 0.10	9.79 ± 0.10	9.73 ± 0.27	9.62 ± 0.30
		Disk	19.63	18.44	1.19	10.29 ± 0.10	9.74 ± 0.10	9.53 ± 0.27	9.52 ± 0.29
779	*B, I*	Disk	20.64	19.65	0.99	10.06 ± 0.10	9.51 ± 0.10	9.16 ± 0.27	9.18 ± 0.28
781	*B, I*	Host	20.29	19.14	1.15	10.79 ± 0.10	10.24 ± 0.10	10.00 ± 0.27	9.98 ± 0.29
		Bulge	21.05	19.76	1.30	10.55 ± 0.10	10.00 ± 0.10	9.86 ± 0.27	9.79 ± 0.30
		Disk	21.06	20.06	1.01	10.43 ± 0.10	9.88 ± 0.10	9.54 ± 0.27	9.54 ± 0.29
782	*B, I*	Host	20.08	18.94	1.14	11.20 ± 0.10	10.65 ± 0.10	10.40 ± 0.27	10.39 ± 0.30
		Bulge	22.52	20.98	1.54	10.38 ± 0.10	9.83 ± 0.10	9.87 ± 0.27	9.67 ± 0.31
		Disk	20.22	19.14	1.08	11.12 ± 0.10	10.56 ± 0.10	10.28 ± 0.27	10.31 ± 0.30
790	*B, I*	Host	19.76	18.41	1.35	10.99 ± 0.10	10.43 ± 0.10	10.34 ± 0.27	10.26 ± 0.30
		Bulge	19.96	18.65	1.31	10.89 ± 0.10	10.34 ± 0.10	10.21 ± 0.27	10.10 ± 0.30
		Disk	21.86	19.94	1.91	10.37 ± 0.10	9.82 ± 0.10	10.12 ± 0.27	9.76 ± 0.33
840	*B, I*	Host	19.44	18.14	1.30	11.12 ± 0.10	10.57 ± 0.10	10.44 ± 0.27	10.38 ± 0.30
		Bulge	20.41	18.95	1.46	10.79 ± 0.10	10.24 ± 0.10	10.22 ± 0.27	10.12 ± 0.31
		Disk	20.01	18.86	1.15	10.83 ± 0.10	10.28 ± 0.10	10.04 ± 0.27	10.04 ± 0.29

Note. Magnitudes are reported in AB magnitudes and color refers to either *B–I* or *B–R*. The last column lists the stellar masses estimated with `CIGALE` to compare with our fiducial stellar masses.

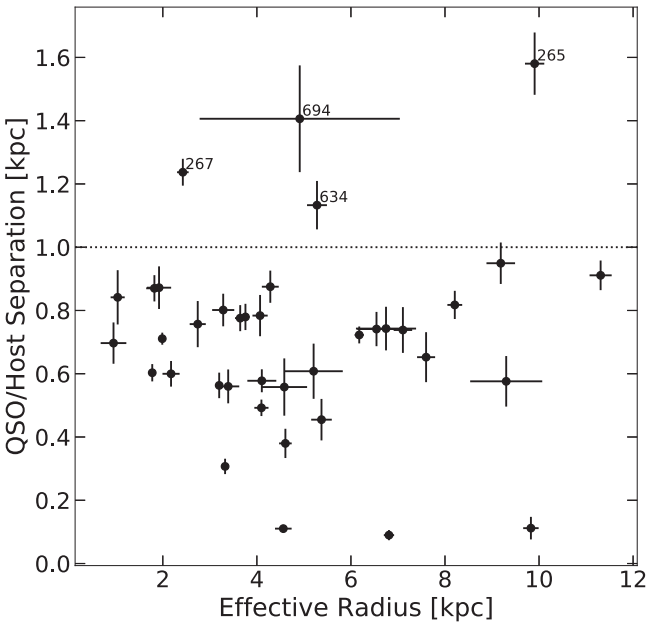

Figure 3. Projected physical offset between the quasar position and host centroid in the IR images as a function of the host effective radius. The uncertainties are estimated from GALFIT (quasar position and effective radius) and the quasar-subtracted host images (centroid position of the host). The error bars are inflated by a factor of 10 for clarity, as the GALFIT uncertainties are small and likely underestimated (median uncertainties are ∼0.02 kpc for the quasar/host separation and ∼0.005 kpc for the effective radius).

the centroid measurements of the host galaxy. These results suggest that $z < 1$ quasars are well centered within ∼1 kpc of the host centroid, consistent with the findings using alternative approaches (Shen et al. 2019).

While studies of local AGNs have demonstrated that BH properties mainly correlate with the bulge and not the entire host (e.g., Kormendy & Ho 2013), studies at higher redshift are often limited to the BH–host relations when bulge/disk decomposition is difficult or impossible (e.g., Jahnke et al. 2009; Merloni et al. 2010). In this work, we present both the BH–bulge and BH–host relations in our sample, where $M_{*,\rm bulge}$ and $M_{*,\rm host}$ refer to the bulge-only and total host stellar mass, respectively. We include all sources in the $M_{\rm BH}$–$M_{*,\rm host}$ relation and exclude the disk-only (PSF+disk) objects in the $M_{\rm BH}$–$M_{*,\rm bulge}$ relation. When comparing with earlier work, we examine their bulge/disk decomposition assumptions and place the comparison on an equal footing, i.e., including bulge-dominated or bulge/disk-decomposed sources only in the $M_{\rm BH}$–$M_{*,\rm bulge}$ relation, and including all sources in the $M_{\rm BH}$–$M_{*,\rm host}$ relation.

3.2. Comparison with Earlier Work

Figure 4 shows the $M_{\rm BH}$–$M_{*,\rm host}$ and $M_{\rm BH}$–$M_{*,\rm bulge}$ relations of our sample and several local and higher-redshift samples. High-resolution HST imaging has been used to investigate the AGN host galaxies at $z > 0.2$ (e.g., Jahnke et al. 2009; Bennert et al. 2011; Bentz & Manne-Nicholas 2018; Ding et al. 2020). Similar to our study, bulge/disk decomposition is only possible for a small subset of these nonlocal samples. We follow the approach of Jahnke et al. (2009), Bennert et al. (2011), and Bentz & Manne-Nicholas (2018) and assume $M_{*,\rm bulge} \approx M_{*,\rm host}$ when there is no evidence of additional components, which differs from Ding et al. (2020), who estimated $M_{*,\rm bulge}$ by assigning bulge/total ratios depending on the Sérsic indices of the host profile.

At even higher redshift (e.g., $z \gtrsim 1.5$), host stellar masses can be obtained by SED fitting (e.g., Merloni et al. 2010; Dong & Wu 2016; Suh et al. 2020) or imaging analysis of lensed quasars (Peng et al. 2006b; Ding et al. 2021). SED fitting with wide wavelength coverage can provide better color information for estimating the stellar masses (compared to using only two HST bands), and large samples can be studied simultaneously in multiwavelength fields. However, it is impossible to distinguish between the bulge and disk components through SED fitting. $M_{*,\rm host}$ can also be measured from the reconstructed images of strongly lensed quasars up to $z \sim 3$. Our sample is generally consistent with the $M_{\rm BH}$–$M_{*,\rm bulge}$ and $M_{\rm BH}$–$M_{*,\rm host}$ relations of these intermediate-to-high-redshift samples.

Our sample is the only uniformly selected (i.e., selected based on a flux limit) AGN sample with RM-based BH masses to study the BH scaling relations beyond the local universe ($z > 0.1$). The RM masses in Grier et al. (2017b) are consistently calibrated to the BH–host relations in quiescent local galaxies in Kormendy & Ho (2013) using the virial factor from Woo et al. (2015). BH masses in all the comparison samples, except for Bentz & Manne-Nicholas (2018), are derived from the SE method, which is less reliable than RM masses. The SE method relies on a "tight" R–L relation to estimate BLR sizes based on quasar luminosities; however, recent studies (Du et al. 2016; Fonseca Alvarez et al. 2020) have shown that the local R–L relation is biased toward the local AGN sample and could be overestimating SE BH masses by as much as ∼ 0.3 dex when applying to the general quasar population. Maithil et al. (2022) showed that SE masses are overestimated and accretion rate measurements (e.g., Eddington ratio) are underestimated for high-accreting AGNs by comparing the local R–L relation to the "Fe-corrected" R–L relation (Du & Wang 2019). Finally, the SE method is calibrated to local quiescent galaxies or local RM AGNs, and different virial factors may be used for different samples or broad-line species. When comparing to samples from the literature, we rescale all $M_{\rm BH}$ values using $f = 4.47$ as in Grier et al. (2017b), even for the SE masses.

We also compare our results with local baseline samples from the literature, including the quiescent galaxies (mainly ellipticals; Kormendy & Ho 2013), active galaxies (Bennert et al. 2021), and RM AGNs (Bentz & Manne-Nicholas 2018). The $M_{\rm BH}$–$M_{*,\rm bulge}$ and $M_{\rm BH}$–$M_{*,\rm host}$ relations of the three local samples and our best-fit relations are consistent in slope and intercepts within uncertainties. However, Reines & Volonteri (2015) find that AGN hosts follow similar slopes to those of local quiescent galaxies but are an order of magnitude lower in normalization for the $M_{\rm BH}$–$M_{*,\rm host}$ relation. They suggested that the difference in normalization may be due to AGN activity or galaxy morphology (which is also shown in Greene et al. 2020). These results may appear contradictory at first glance; however, it is difficult to provide a straightforward comparison since these studies adopt different stellar mass estimation methods. Bentz & Manne-Nicholas (2018) also observed a difference in normalization using the Bell & de Jong (2001) CMLR, but not when they use the Into & Portinari (2013) CMLR, which is the same CMLR adopted in this work. Due to different assumptions in the CMLR relations, we do not

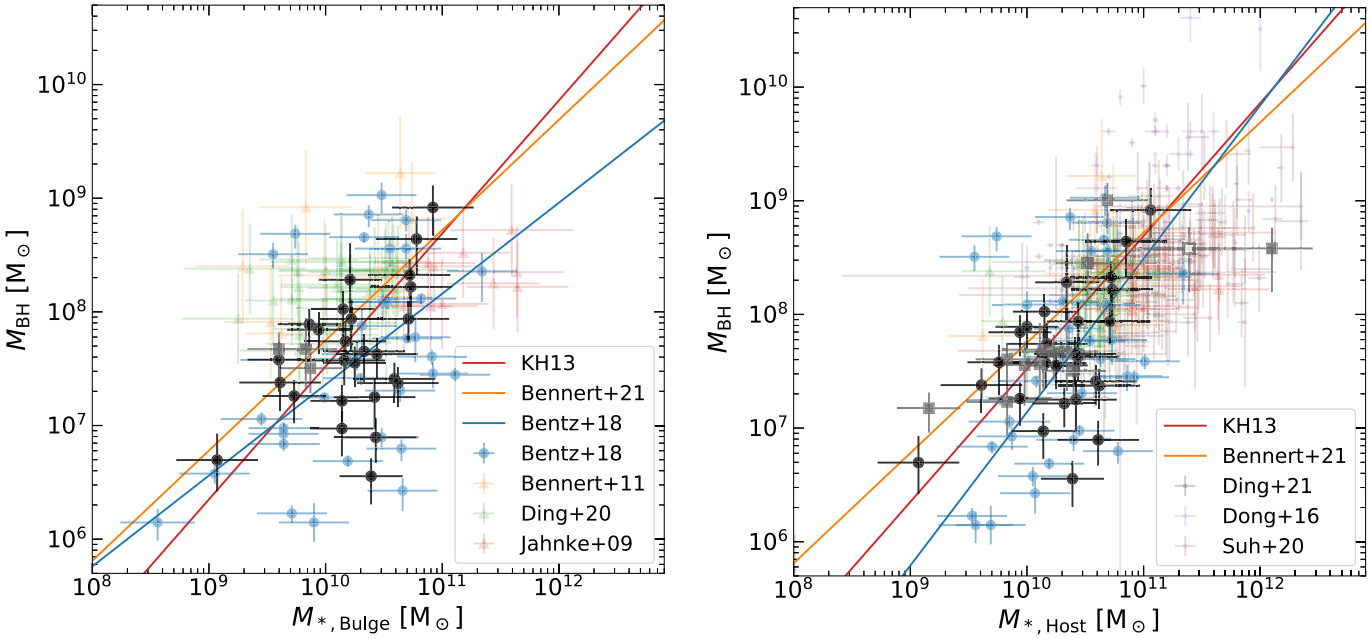

Figure 4. Comparison with literature samples. Our sample is shown with black circles (bulge dominated) and gray squares (disk dominated), and the open gray square is the CIGALE stellar mass of RM265. The blue circles are the local RM sample from Bentz & Manne-Nicholas (2018). The triangles show the high-redshift samples with HST imaging (orange: Bennert et al. 2011, median redshift $z_{med} = 1.2$; green: Jahnke et al. 2009, $z_{med} = 1.3$; red: Ding et al. 2020, $z_{med} = 1.5$), and the circles indicate the high-redshift samples with SED fitting (purple: Ding et al. 2021, $z_{med} = 1.7$; brown: Dong & Wu 2016, $z_{med} = 1.1$; pink: Suh et al. 2020, $z_{med} = 1.6$). The solid lines show the best-fit relations of the local quiescent galaxy (red; Kormendy & Ho 2013), active galaxy (orange; Bennert et al.2021), and RM AGN (blue; Bentz & Manne-Nicholas 2018).

compare the Reines & Volonteri (2015) relation, which uses the Zibetti et al. (2009) CMLR, with our results directly.

Sijacki et al. (2015) and Mutlu-Pakdil et al. (2018) studied the M_{BH}–$M_{*,bulge}$ and M_{BH}–$M_{*,host}$ relations in the Illustris simulation. Sijacki et al. (2015) found that, at $z \sim 0$, the M_{BH}–$M_{*,bulge}$ relation is tight at the high-BH/galaxy mass end, but scatter increases below $M_{BH} \sim 10^8\ M_\odot$, similar to the general trend of our sample. Their bulge mass is defined by the total stellar mass within the stellar half-mass radius and not by morphology or kinematics. The difference in scatter in the high/low-mass end might suggest different evolutionary paths or feedback mechanisms for establishing the BH scaling relations. Local studies of BH scaling relations also found that late-type galaxies follow a similar slope in the BH scaling relations, but at a lower normalization than early-type galaxies (Reines & Volonteri 2015; Greene et al. 2020; Zhao et al. 2021). In addition, there is no strong evolution in the M_{BH}–$M_{*,bulge}$ relation up to $z \sim 1$ in the Illustris simulation. Mutlu-Pakdil et al. (2018) studied the M_{BH}–$M_{*,host}$ relations in the Illustris simulation to provide a better comparison for high-redshift observations and reported that the M_{BH}–$M_{*,bulge}$ and M_{BH}–$M_{*,host}$ relations are generally consistent with each other up to $z \sim 1$. Volonteri et al. (2016) studied the M_{BH}–$M_{*,host}$ and M_{BH}–$M_{*,bulge}$ relations in the Horizon-AGN simulation. By identifying classical bulges in their simulation through kinematics and bulge/disk decomposition, they reproduced the tight M_{BH}–$M_{*,bulge}$ relation of classic bulges from Kormendy & Ho (2013). Other simulations, e.g., MassiveBlack-II (Khandai et al. 2015), generally produce similar trends in BH scaling relations at $z < 1$. Habouzit et al. (2021) performed a systematic analysis on the evolution of M_{BH}–M_* relations in cosmological simulations of Illustris, TNG 100, TNG 300, Horizon-AGN, EAGLE, and SIMBA. They find that the median/mean M_{BH}–M_* relations at $0 < z < 1$ are in general agreement with observational data and that there is little evolution with redshift. The observed tight correlation between the sample-averaged BH accretion rate and star formation at $0.5 < z < 3$ indicates that the growth of BHs and that of host galaxies are in sync, and the BH scaling relations should not have strong redshift dependence (Yang et al. 2019). However, the scatter in M_{BH}–M_* relations differs in these simulations, which mainly depends on the implemented subgrid physics in the simulations, e.g., the strength and efficiency of supernova and AGN feedback.

3.3. M_{BH}–$M_{*,host}$ and M_{BH}–$M_{*,bulge}$ Relations of Our Sample

Our sample consists of 38 sources spanning more than two orders of magnitude in M_{BH} and $M_{*,host/bulge}$, which is sufficient for statistical analysis. The Pearson correlation coefficient r between M_{BH} and $M_{*,host}/M_{*,bulge}$ is roughly 0.5, suggesting that the BH and galaxy/bulge masses are positively correlated. The low p-values indicate that the M_{BH}–$M_{*,host}$ and M_{BH}–$M_{*,bulge}$ correlations are statistically significant at the 3.9σ and 2.5σ levels. We use the LINMIX_ERR algorithm (Kelly 2007) to perform linear regression fitting on the M_{BH}–$M_{*,bulge}$ and M_{BH}–$M_{*,host}$ relations. LINMIX_ERR is a Bayesian fitting algorithm that accounts for uncertainties in both axes and intrinsic scatter in the relations. We fit for the equation

$$\log \frac{M_{BH}}{M_\odot} = a + b \times \log\left(\frac{M_*}{10^{10}\ M_\odot}\right) \quad (2)$$

in Figure 5 and tabulate the best-fit parameters in Table 4.

The regression fits to the observed samples do not account for selection effects. In Section 4.3 we use a more robust fitting code to constrain the intrinsic BH–host scaling relations, and we include the bias-corrected best-fit parameters in Table 4. However, given the large dynamic range of our sample,

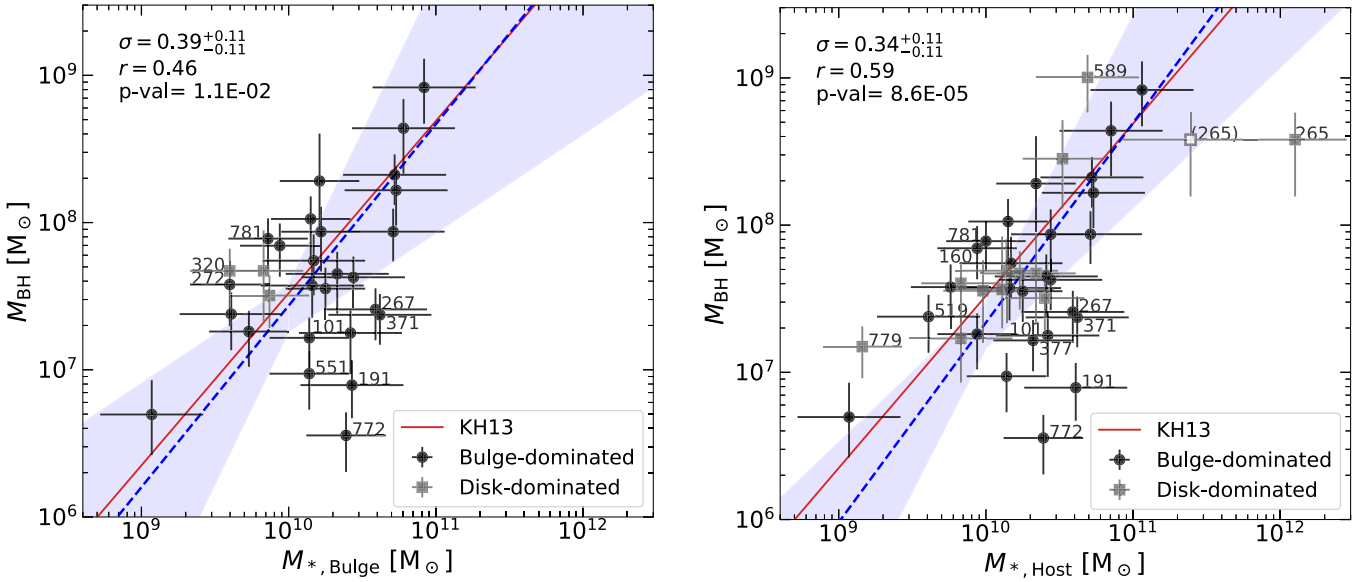

Figure 5. BH mass as functions of bulge stellar mass (left) and total stellar mass (right) of our sample (black circles for bulge-dominated sources, gray squares for disk-dominated sources, and the open gray square for the CIGALE stellar mass of RM265). The blue dashed lines (and the gray shaded areas) are the best-fit relation (1σ range) of our sample. The red solid lines are the Kormendy & Ho (2013) local M_{BH}–$M_{*,\,bulge}$ relation. The Pearson r coefficient, p-value, and intrinsic scatter of the relations are labeled in the upper left corner of each panel.

selection effects do not appear to impact the results significantly, as we will show in Section 4.3.

3.4. Comparison with Spectral Decomposition

We compare the host light fraction and total stellar mass derived from HST imaging decomposition in this work and the spectral decompositions in Shen et al. (2015b) and Matsuoka et al. (2015). Both of these earlier studies measured host galaxy properties using the high signal-to-noise ratio coadded spectra from the first-year SDSS-RM spectra (Shen et al. 2015a). Shen et al. (2015b) used a principal component analysis method to decompose coadded spectra into quasar and galaxy spectra and measured host galaxy properties directly from the galaxy spectra, including stellar velocity dispersion and host-free AGN luminosity. Matsuoka et al. (2015) performed spectral decomposition on the coadded spectra using models of AGN and galaxy spectra and measured host galaxy properties by fitting the decomposed galaxy spectra with stellar population models.

To compare the host light fraction (f_*, the fractional contribution of the host stellar component to the total flux), we calculate the host fraction in the HST imaging using the decomposed GALFIT models within the 2″ diameter spectral aperture, and we calculate the host fraction in spectral decomposition by computing the expected flux in the F606W and F814W bandpass in the decomposed spectra from Shen et al. (2015b). Figure 6 (left panel) reveals that the host fraction from image decomposition is systematically higher than that derived from spectral decomposition, similar to our finding in the pilot study (Li et al. 2021c) and in Yue et al. (2018). Figure 6 (right panel) compares the host stellar mass derived from this work and that from Matsuoka et al. (2015). Our stellar mass is systematically smaller by ∼0.5 dex. The cause of the stellar mass offset is currently unclear, but it might be partially due to different choices of initial mass functions and stellar population models in Matsuoka et al. (2015) and CIGALE, or the fiber-loss correction applied in Matsuoka et al. (2015), which assumes that the mass-to-luminosity ratio in the central region (within the 2″-diameter aperture) represents that for the entire galaxy.

Table 4
Best-fit Parameters of the Scaling Relations

Scaling Relations	a	b	σ
Bulge (original)	$7.44^{+0.13}_{-0.16}$	$1.18^{+0.76}_{-0.52}$	$0.39^{+0.11}_{-0.11}$
Host (original)	$7.34^{+0.14}_{-0.17}$	$1.36^{+0.59}_{-0.40}$	$0.34^{+0.11}_{-0.11}$
Bulge (bias-corrected)	$7.03^{+0.26}_{-0.41}$	$1.67^{+0.83}_{-0.72}$	$0.59^{+0.23}_{-0.21}$
Host (bias-corrected)	$7.01^{+0.23}_{-0.33}$	$1.74^{+0.64}_{-0.64}$	$0.47^{+0.24}_{-0.17}$

4. Biases in the Observed Black Hole Scaling Relations

4.1. Sources of Biases

The parent SDSS-RM sample is subjected to the Lauer et al. (2007) bias, which is the statistical bias in flux-limited samples due to intrinsic scatter in the scaling relation. Since the sample selection is well understood for the parent SDSS-RM sample (i.e., a uniform magnitude cut in i band), we demonstrate the selection effects caused by the flux limit in Section 4.2 and correct for the selection bias through computational methods in Section 4.3.

Our sample selection also depends on successful RM lag measurements, which may depend on survey design (monitoring cadence and duration), BH properties (mass and Eddington ratio), etc. In general, lags shorter than the observing cadence and lags longer than (a fraction of) the monitoring duration are difficult to detect. However, simulations also showed that lags could be recovered without significant bias when combining multiple lag detection methods and reasonable lag significance criteria (Li et al. 2019). The deviation between the SDSS-RM R–L relation (Grier et al. 2017b) and the local R–L relation (Bentz et al. 2013) may not be entirely due to observational biases, but partly to actual difference in the quasar parameters probed (Li et al. 2019; Fonseca Alvarez et al. 2020), and the

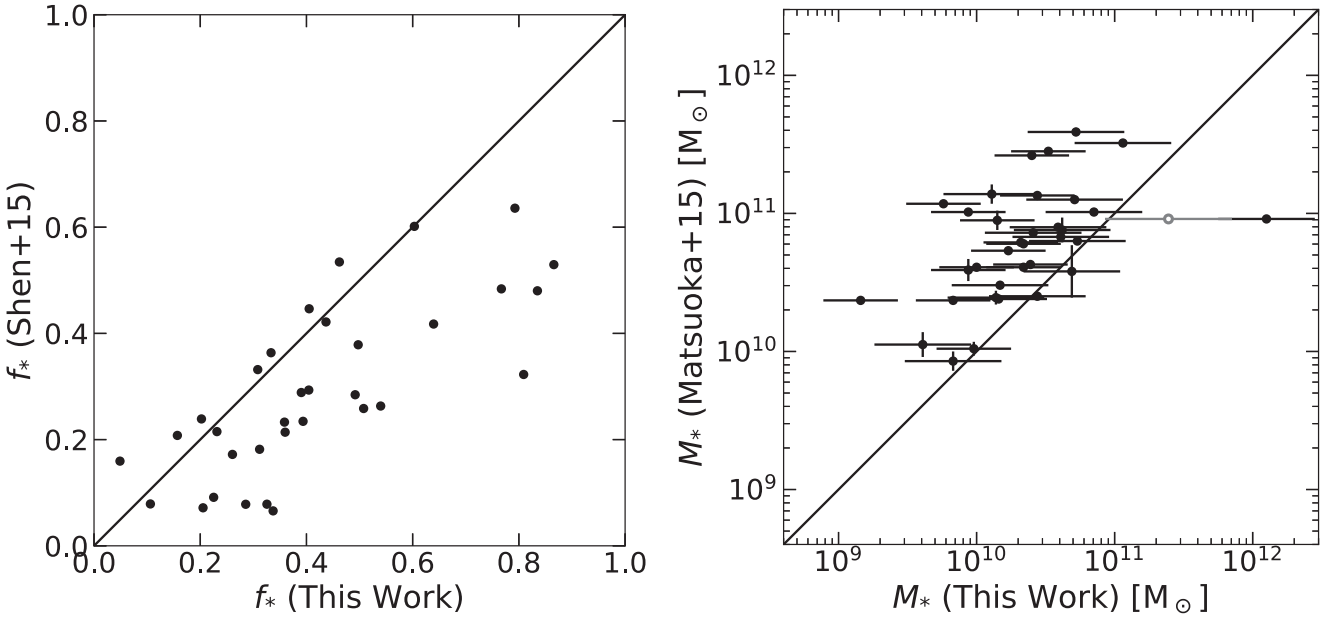

Figure 6. Left: comparison of the derived host light fraction from this work and Shen et al. (2015b), both measured in the UVIS (F606W or F814W) bandpass. The black dashed line shows the 1:1 ratio line. Right: comparison of the total stellar masses derived from this work and Matsuoka et al. (2015) for overlapping objects.

SDSS-RM parent sample is a better representation of the general quasar population (Shen et al. 2015a). Since the lag detection fraction in the parent SDSS-RM sample is nearly uniform up to $z \sim 0.8$, we assume that the sample selection is not strongly affected by additional selection biases based on the quasar properties or survey design.

Our scaling relations are based on RM BH masses, so they avoid the SE mass bias (Shen & Kelly 2010), which originates from the combination of luminosity-dependent scatter in the SE BH mass estimates, the sample flux limit, and the underlying true BH mass distribution. However, the uncertainties of our RM BH masses are likely underestimated without considering the intrinsic scatter in the virial factor for individual objects (e.g., ∼0.3–0.4 dex; Shen et al. 2023). In addition, even with high-resolution HST images, it is extremely difficult to resolve the bulges (or other galaxy structures), adding uncertainties in the bulge identification and mass estimation (see discussion in Section 5.2). If the uncertainties in $M_{\rm BH}$ and M_* are underestimated, the intrinsic scatter of the observed scaling relations is likely overestimated, since the "true" intrinsic scatter is buried in measurement uncertainties. Nonetheless, as long as the extents of underestimation in $M_{\rm BH}$ and M_* uncertainties are not correlated with the BH/galaxy properties, the slope and normalization of the observed scaling relation should remain unbiased.

4.2. Selection Effects in Flux-limited Samples

To illustrate selection biases in our flux-limited sample due to the Lauer bias, we perform a forward-modeling simulation following the procedures in Shen et al. (2015b). We first simulate a parent quasar sample following the local M_* distribution from Bernardi et al. (2010) and the $M_{\rm BH}$–$M_{*,\rm bulge}$ relation from Kormendy & Ho (2013), with an intrinsic scatter of 0.29 dex. Using the true $M_{\rm BH}$, we assign a quasar bolometric luminosity by assuming a lognormal Eddington ratio distribution ($\lambda \equiv L_{\rm bol}/L_{\rm Edd}$), and the Eddington luminosity is $L_{\rm Edd} = 1.26 \times 10^{38} (M_{\rm BH}/M_\odot)$ erg s^{-1}. We choose a mean Eddington ratio of $\langle \log \lambda \rangle = -1$ and a scatter of 0.3 dex (Shen et al. 2008; Shen & Kelly 2012). We include measurement uncertainties of 0.35 dex for M_* and 0.2 dex for $M_{\rm BH}$ to mimic the uncertainty levels of our CMLR-based M_* and RM $M_{\rm BH}$ measurements. Finally, for 100 bootstrap iterations, we randomly draw 38 sources to perform `LINMIX_ERR` fitting at different i-mag < 16, 19, and 22 (similar to the flux limit of the SDSS-RM sample).

Figure 7 shows how the flux limit biases the observed scaling relations. When the flux limit increases, overmassive BHs are preferentially selected, the slope of the best-fit relation becomes shallower, and the normalization increases. The best-fit intrinsic scatter remains roughly the same in our simulations. However, our simulation does not include the outlier population with undermassive BHs seen in observations (see, e.g., Figure 4). Missing the outlier population could lead to an underestimation of the intrinsic scatter and bias due to the flux limit, since undermassive BHs are less likely to be selected in flux-limited surveys. However, if included in the observed sample, undermassive BHs may on average have higher accretion rate and shorter lags, which are favorable for detection in a short monitoring campaign with sufficient cadence. Given the relatively faint flux limit of our SDSS-RM sample, selection biases do not play an important role in the measured $M_{\rm BH}$–M_* relations (see the right panel of Figure 7), and we found relations at $z_{\rm med} = 0.5$ similar to the local relations. Our results are consistent with other studies that properly account for selection biases (e.g., Sexton et al. 2019; Suh et al. 2020; Li et al. 2021a).

4.3. Quantifying the Selection Effects

To quantitatively account for the underlying galaxy properties (i.e., the galaxy mass function) and selection effects, we follow the framework of Kelly (2007) to perform a Markov Chain Monte Carlo (MCMC) fitting for the intrinsic scaling relations and scatters. Specifically, we wrote an MCMC fitting code based on the Metropolis–Hastings algorithm (Metropolis

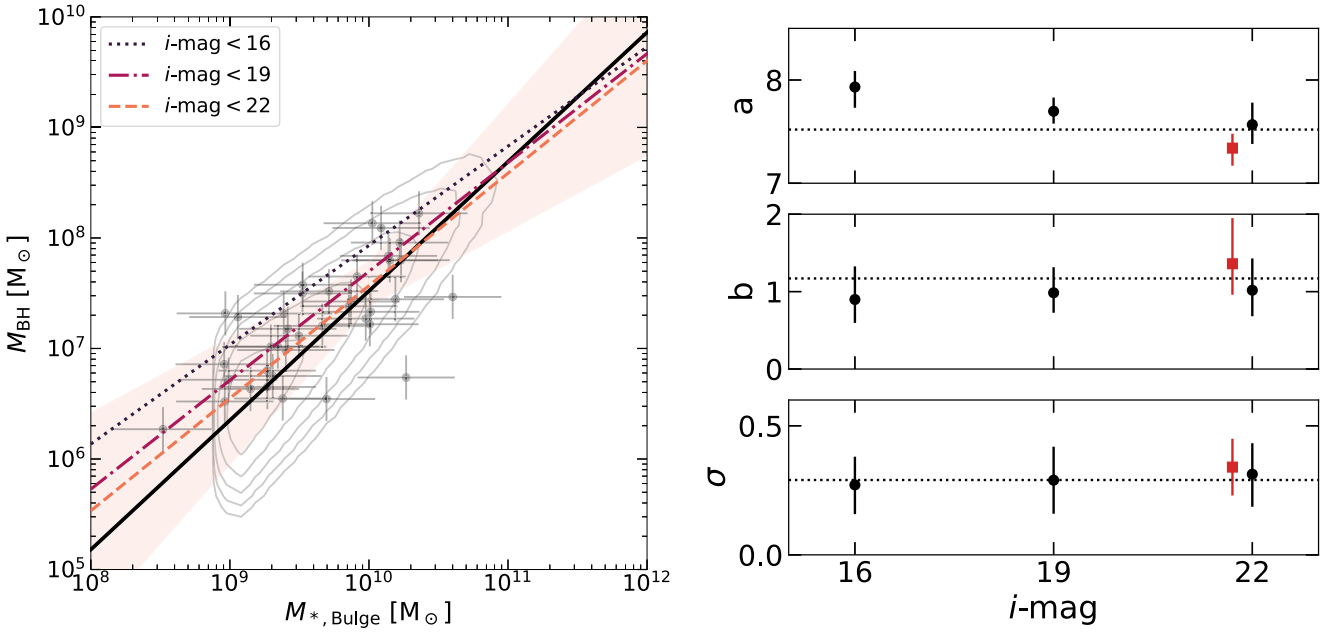

Figure 7. Results of the Lauer et al. (2007) bias simulation described in Section 4.1. Left: gray contours represent the underlying quasar sample, and the gray points are one realization of the mock sample at the $i = 22$ flux limit, after being perturbed with measurement uncertainties. The black solid line is the unbiased Kormendy & Ho (2013) relation. The colored lines indicate the results of the mock sample at different flux limits. Right: the best-fit M_{BH}–$M_{*,bulge}$ parameters at each flux threshold and the best-fit M_{BH}–$M_{*,host}$ parameters of our sample (plotted in red at $i = 21.7$). The dotted lines show the parameters and intrinsic scatter from the Kormendy & Ho (2013) relation.

et al. 1953; Hastings 1970) and the statistical derivation in Sections 4.1 and 5.1 of Kelly (2007), which allows us to account for the selection effect based on the dependent variable. Here we briefly summarize the fitting algorithm and parameter setup and refer the readers to Kelly (2007) for the full, detailed mathematical derivation. Our custom fitting code is available via ftp://quasar.astro.illinois.edu/public/sdssrm/paper_data/Li_2023_HST_host.

As shown in Kelly (2007), when the intrinsic scatter and the uncertainties are comparable to the dynamical range of the data, the best-fit slope becomes shallower when the underlying distribution is not considered as a prior in the fitting procedure. One solution is to incorporate empirical distributions into the likelihood function, e.g., the observed local stellar mass function $\Phi(x)$ from the literature (e.g., Bernardi et al. 2010). However, due to the limited dynamical range in M_* and the small sample size of our data, the local galaxy mass function is not a good prior for our sample. Alternatively, Kelly (2007) suggests using a series of Gaussian functions to model the underlying distribution, which provides a flexible and empirical solution even when the underlying distribution is unknown. This is the method implemented in the original `LINMIX_ERR` fitting algorithm, which we continue to adopt in our MCMC fitting for consistency.

When the sample selection is based on the dependent variable (i.e., M_{BH}), the posterior distribution and likelihood depend on an additional term ($P(I = 1|\theta)$, where θ are the model parameters) that describes the likelihood of including each data point in the observed sample based on the model parameters (for more details, see Section 5.1 in Kelly 2007). Following the same procedure as described in the first paragraph of this section, we estimate the expected i-band magnitude by assigning a random Eddington ratio and an Eddington luminosity based on the redshift and a range of "true" M_{BH} for each data point. The probability of including a data point is 1 if i-mag < 21.7 and 0 if i-mag > 21.7. Finally, we calculate $P(I = 1|\theta)$ by integrating the probability of including each data point and their likelihood over a range of "true" M_{BH} and M_* given the model parameters. We adopt uninformative, flat priors for all parameters ($5 < a < 10$, $0 < b < 3$, and $0.0001 < \sigma^2 < 1$) and minimize the product of the likelihood and prior to compute the posterior distribution of the parameters a, b, and σ.

Figures 8 and 9 present the posterior distribution of a, b, and σ, and the best-fit values are tabulated in Table 4. As expected, the slope of the intrinsic scaling relations becomes steeper, and the normalization decreases, after correcting for the selection biases. The best-fit parameters are within uncertainties as the `LINMIX_ERR` fit (without considering selection bias) discussed in Section 3, demonstrating that our results are not strongly affected by selection biases.

Intrinsic scatter of the M_{BH}–$M_{*,bulge}$ and M_{BH}–$M_{*,host}$ relations is an important indicator for BH–galaxy coevolution, as it might be related to the galaxy/AGN properties and their evolutionary path. The local samples of Kormendy & Ho (2013) and Bennert et al. (2021) only include classical bulges and pseudobulges and have a smaller intrinsic scatter of 0.28–0.39 dex. However, when including all morphological types and active/inactive galaxies, the intrinsic scatter increases to ∼0.5 dex (Reines & Volonteri 2015; Bentz & Manne-Nicholas 2018) for the M_{BH}–$M_{*,bulge}$ relation and becomes even slightly larger for the M_{BH}–$M_{*,host}$ relation. In addition, the BH accretion rate is found to be correlated with other host properties, e.g., compactness of the central ∼1 kpc region (Ni et al. 2019, 2021), which can introduce additional scatter in the BH scaling relations.

For our quasar sample, the intrinsic scatters of the M_{BH}–$M_{*,host}$ and M_{BH}–$M_{*,bulge}$ relations are $0.47^{+0.24}_{-0.17}$ dex

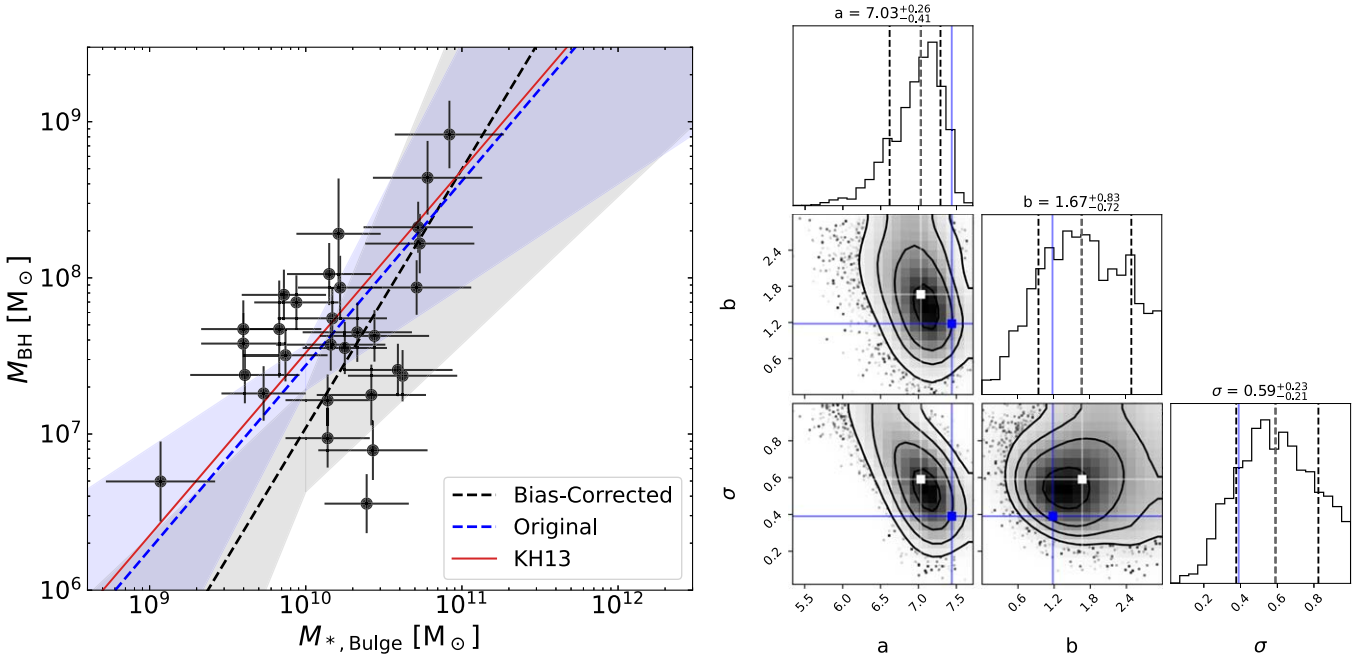

Figure 8. MCMC fitting for the M_{BH}–$M_{*,bulge}$ relation when considering the selection bias. Left: the M_{BH}–$M_{*,bulge}$ relation with the 1σ range drawn from the posterior (black dashed line and shaded area). The blue dashed lines and shaded area show the original best-fit relations from LINMIX_ERR (previously shown in Figure 5), and the red solid line is the local M_{BH}–$M_{*,bulge}$ relation from Kormendy & Ho (2013). Right: the posterior distribution of the parameters a, b, and σ. The best-fit parameters from LINMIX_ERR and the MCMC fitting are indicated by the blue and white squares, respectively. The MCMC fitting recovers a similar BH–galaxy relation to the original linear regression, indicating that the selection effects are minimal.

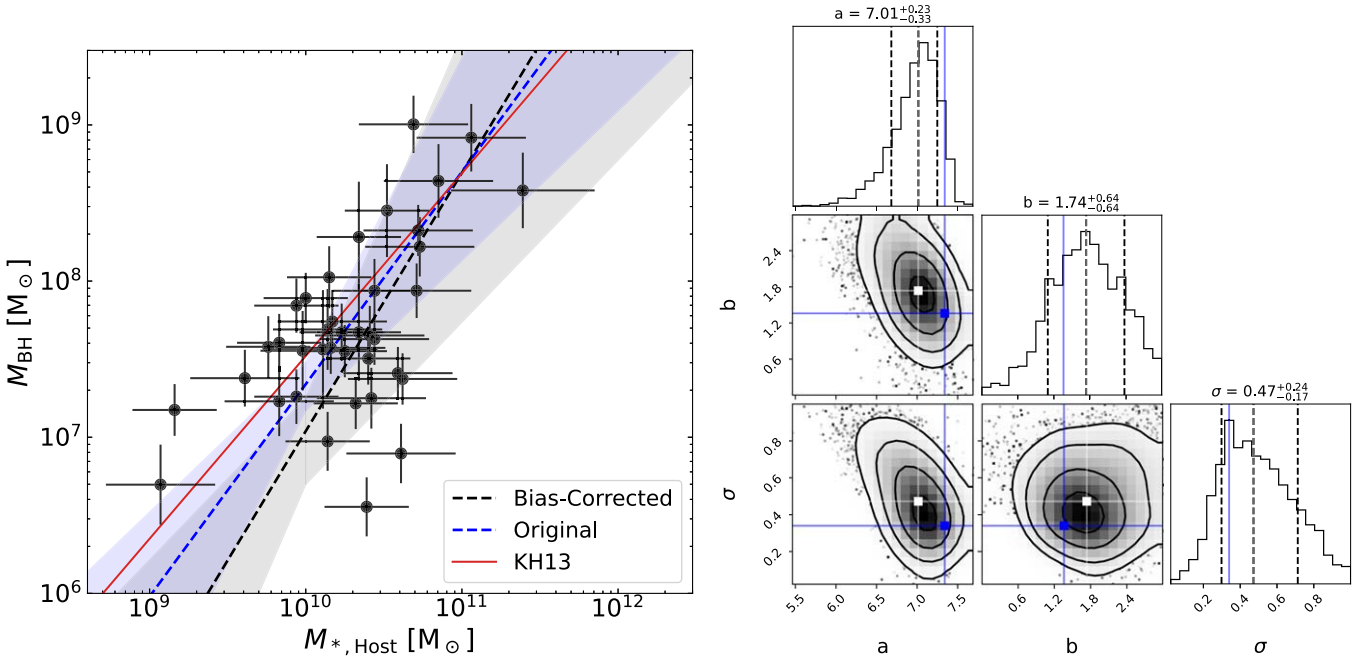

Figure 9. Same format as Figure 8, but for the M_{BH}–$M_{*,host}$ relation.

and $0.59^{+0.23}_{-0.21}$ dex, respectively, after accounting for the selection effects, which are comparable to the scatter in the local relations. The intrinsic scatter of our M_{BH}–$M_{*,host}$ relation is slightly smaller ($\lesssim 0.5\sigma$ of difference) than our M_{BH}–$M_{*,bulge}$ relation, which we will further discuss in Section 5.2. Because we have neglected the systematic uncertainty in our RM BH masses due to the scatter in individual virial coefficients, the actual intrinsic scatter in the BH–host stellar mass relations for $0.2 < z < 0.8$ quasars might be even smaller.

5. Discussion

5.1. Evolution of Black Hole Scaling Relations

Earlier works on M_{BH}–$M_{*,bulge}$ and M_{BH}–$M_{*,host}$ relations found that the average BH/host galaxy mass ratio evolves

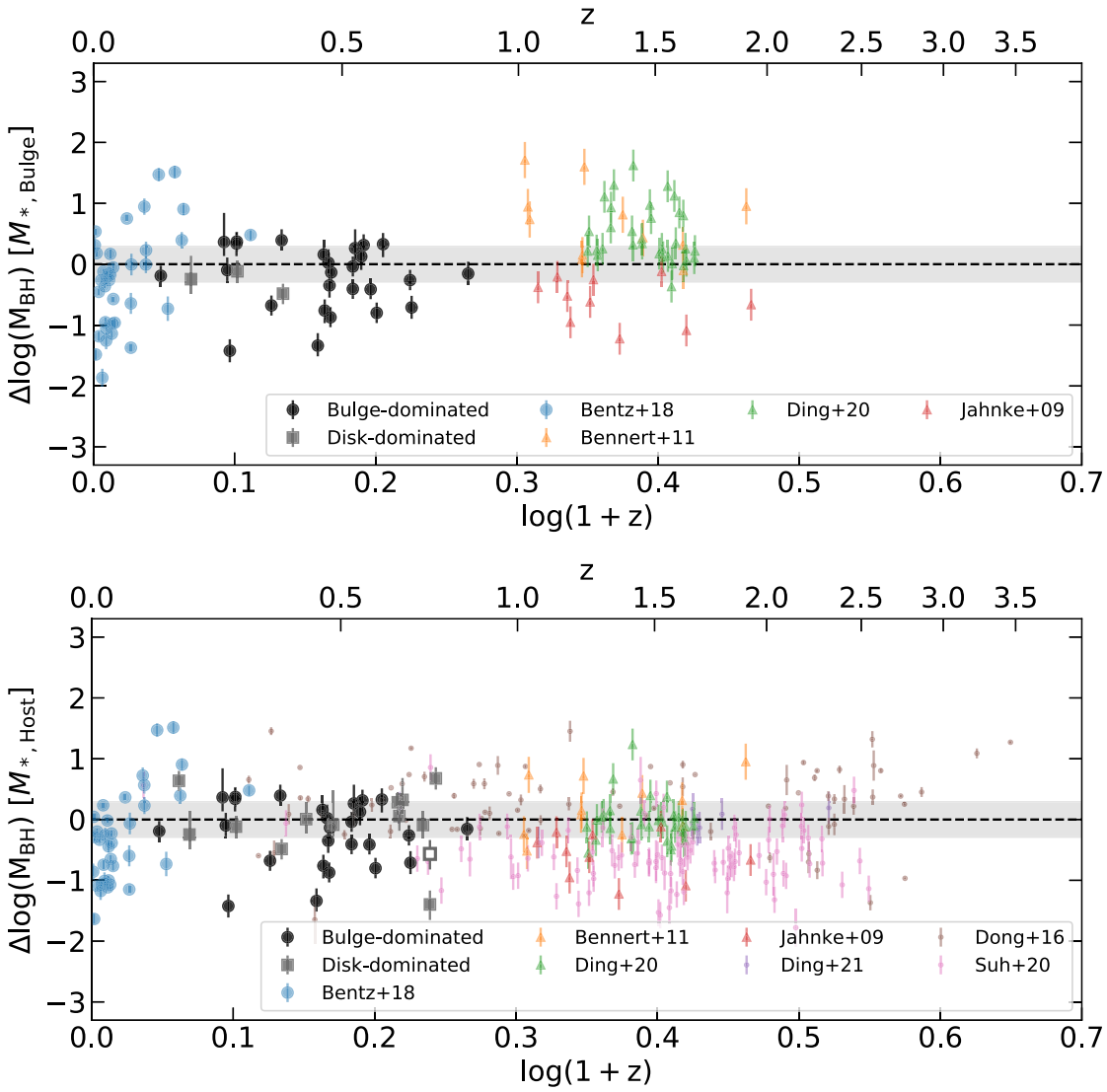

Figure 10. The deviation of the measured BH masses from the expected BH masses estimated based on the local Kormendy & Ho (2013) $M_{\rm BH}$–$M_{\rm Bulge}$ relation ($\Delta\log(M_{\rm BH})$), as a function of redshift. The top (bottom) panel shows the deviation estimated by the bulge (total) masses. There is no obvious trend in $\Delta\log(M_{\rm BH})$ with redshift, indicating negligible redshift evolution in the BH–host relations. Our work is the only sample with RM-based BH masses beyond $z > 0.3$, and all other samples beyond $z > 0.3$ are based on SE BH masses. Vertical error bars are from uncertainties in BH mass only.

positively with redshift (Peng et al. 2006a, 2006b; Bernardi et al. 2010; Merloni et al. 2010). However, selection biases and measurement uncertainties could yield false positives of the evolution. For example, Jahnke et al. (2009) reported that there is no evidence of evolution when they carefully choose their sample to avoid selection biases. Similarly, Suh et al. (2020) found that the redshift evolution seen in Merloni et al. (2010) can be explained by the Lauer bias (Lauer et al. 2007), and there is no trend of evolution in their X-ray-selected, lower-luminosity sample. Using over 500 uniformly selected $0.2 < z < 0.8$ SDSS quasars, Li et al. (2021a) found a redshift evolution of the offset in the $M_{\rm BH}$–$M_{*,\ \rm host}$ relation that is within ± 0.2 dex from zero, consistent with no significant evolution since $z \sim 0.8$.

Figure 10 presents the deviation of $M_{\rm BH}$ from the Kormendy & Ho (2013) $M_{\rm BH}$–$M_{*,\ \rm bulge}$ relation of our sample. We fit the deviation as a function of log(z), and the slopes and intercepts are consistent with zero, suggesting that there is no redshift evolution from the local relations. The median (16th/84th percentiles) BH/host galaxy mass ratios are $M_{\rm BH}/M_{*,\rm bulge} = 0.0037(0.0007/0.0088)$ and $M_{\rm BH}/M_{*,\rm host} = 0.0030(0.0007/0.0076)$, within 1σ uncertainty of the local value of $M_{\rm BH}/M_{*,\rm bulge} \sim 0.005$ (Kormendy & Ho 2013).

Our results agree with recent observational studies that there is limited evolution in the $M_{\rm BH}$–M_* relation (Suh et al. 2020; Li et al. 2021a). Yang et al. (2019) showed that the sample-averaged BH accretion rate ($\overline{\rm BHAR}$) is primarily correlated with SFR (and not stellar mass) in bulge-dominated galaxies over a wide redshift range of $z = 0.5$–3, suggesting that SMBH and bulge growths are in lockstep, and thus the $M_{\rm BH}$–$M_{*,\rm bulge}$ relation should not evolve with redshift. In addition, the ratio $\overline{\rm BHAR}$/SFR and the slope of their $\overline{\rm BHAR}$−SFR relation are similar to the $M_{\rm BH}/M_{*,\rm bulge}$ ratio and the slope of the $M_{\rm BH}$–$M_{*,\rm bulge}$ relation observed in the local universe.

5.2. Black Hole–Bulge versus Black Hole–Host Relations

In the local universe, SMBH masses are tightly correlated with the properties of classical bulges, but not with disks or total mass of the host galaxy. However, the intrinsic scatter in

the $M_{\rm BH}$–$M_{*,\rm host}$ relation of our sample is slightly smaller than that in the $M_{\rm BH}$–$M_{*,\rm bulge}$ relation. There are a few extra sources of uncertainties for the bulge mass estimate than for the total mass estimate, which will contribute to the intrinsic scatter. First of all, bulge–disk decomposition could add significant uncertainties to the bulge mass. Most of our host galaxies are far less luminous than the quasar, and compact hosts could be near the limit of HST imaging resolution. Bulge–disk decomposition is reliable when both the bulge and disk are sufficiently bright (compared to the central quasar) and there is distinct difference in their effective radii. Furthermore, we cannot distinguish classical bulges from pseudobulges or other bulge-like structures from surface brightness decomposition, nor could we model complex bar, spiral, and merger structures in the bulge–disk decomposition, which increases the uncertainties in bulge identification and mass estimation. Gao & Ho (2017) found that rigorous modeling of bars and innermost structures (e.g., rings and disk breaks near the bulge) is crucial to recovering bulge properties, while the modeling of spiral arms and extended disks has negligible effects. We note that some host galaxies in our sample show clear evidence of bars (e.g., RM320, RM634), which are modeled as bulges ($n = 4$) or disks ($n = 1$) in our analysis, without additional bar structures. Moreover, some host galaxies show clear spiral arm features (e.g., RM371, RM772), indicating the presence of disks, but are modeled as "bulges" ($n = 4$). Previous works (e.g., Greene et al. 2020; Zhao et al. 2021) showed that late-type quasar hosts preferentially scatter below early-type hosts in the $M_{\rm BH}$–$M_{*,\rm bulge}$ relation, which is not seen in our data, suggesting that our bulge–disk decomposition is not as reliable in measuring galaxy morphology. A detailed simulation of bulge–disk decomposition for AGNs with similar host and quasar properties (e.g., AGN/host flux ratio, host effective radius, Sérsic indices, and complex structures) is needed to provide quantitative uncertainty estimation, which is beyond the scope of this work.

Another possible source of uncertainty is the CMLR estimation for bulges. Recent studies have reported that compact regions around the SMBH may have denser interstellar medium, boosted star formation, and complex stellar populations (e.g., Kim & Ho 2019; Ni et al. 2019; Shangguan et al. 2020; Yesuf & Ho 2020; Zhuang & Ho 2020; Molina et al. 2021). Two-band color and the use of the empirical M/L relation may not be sufficient to produce reliable estimates for the bulge stellar mass.

6. Conclusions

We present the $M_{\rm BH}$–$M_{*,\rm bulge}$ and $M_{\rm BH}$–$M_{*,\rm host}$ relations of 38 sources with RM-based BH masses (Grier et al. 2017b) and $0.2 \lesssim z \lesssim 0.8$ (median redshift $z_{\rm med} = 0.5$). Our sample is the first uniformly selected sample with RM-based BH masses at $z > 0.3$ for studying BH–host relations and covers two orders of magnitude in BH mass and host stellar mass. The reliable RM-based BH masses and host mass estimates from HST imaging decomposition, combined with the large sample size and dynamic range in mass, allow one to alleviate selection biases in studying the potential evolution of the BH–host scaling relations. Our scaling relations are consistent with those for local AGNs, quiescent galaxies, and other high-redshift samples, with negligible redshift evolution up to $z \lesssim 1$. As shown in Table 4, the best-fitting intrinsic $M_{\rm BH}$–$M_{*,\rm host}$ relation is $\log(M_{\rm BH}/M_\odot) = 7.01^{+0.23}_{-0.33} + 1.74^{+0.64}_{-0.64} \log\,(M_{*,\rm host}/10^{10}\,M_\odot)$ after correcting for the underlying sample distribution and selection effects. We estimate an intrinsic scatter of $0.59^{+0.23}_{-0.21}$ dex and $0.47^{+0.24}_{-0.17}$ dex in the $M_{\rm BH}$–$M_{*,\ \rm bulge}$ and $M_{\rm BH}$–$M_{*,\ \rm host}$ relations, respectively, which is again consistent with the local BH scaling relations. Since our BH mass uncertainties are likely underestimated, the intrinsic scatter in these scaling relations at $z_{\rm med} = 0.5$ may be even smaller. With our approved Cycle 1 JWST proposal (GO-2057, PI: Shen), we will continue to explore BH–host relations and their redshift evolution up to $z \sim 2$ using quasars with direct RM-based BH masses (Grier et al. 2019).

Acknowledgments

J.I.L. acknowledges support from the Government Scholarship to Study Abroad (GSSA) from the Ministry of Education of Taiwan, the Illinois Space Grant Consortium (ISGC) Graduate Fellowship, and the Eric and Wendy Schmidt AI in Science Postdoctoral Fellowship, a Schmidt Futures program. Y.S. acknowledges support from NSF grants AST-1715579 and AST-2009947. L.C.H. was supported by the National Science Foundation of China (11721303, 11991052, 12233001, 12011540375) and the China Manned Space Project (CMS-CSST-2021-A04, CMS-CSST-2021-A06). W.N.B. acknowledges support from NSF grant AST-2106990. P.B.H. is supported by NSERC grant 2017-05983. Based on observations with the NASA/ESA Hubble Space Telescope obtained from the Data Archive at the Space Telescope Science Institute, which is operated by the Association of Universities for Research in Astronomy, Incorporated, under NASA contract NAS5-26555. Support for program No. HST-GO-15849 was provided through a grant from the STScI under NASA contract NAS5-26555.

The data presented in this paper were obtained from the Mikulski Archive for Space Telescopes (MAST) at the Space Telescope Science Institute. The specific observations analyzed can be accessed via doi:10.17909/7rt1-ts28.

Facilities: HST (WFC3/UVIS, WFC3/IR).

Software: AstroDrizzle, Astropy (Astropy Collaboration et al. 2013; Price-Whelan et al. 2018), CIGALE (Boquien et al. 2019), `GALFIT` (Peng et al. 2010), `LINMIX_ERR` (Kelly 2007), matplotlib (Hunter 2007), Numpy (Oliphant 2006), `photutils` (Bradley et al. 2019), `pysynphot` (Lim et al. 2015), seaborn (Waskom et al. 2017).

Appendix

Figure 11 shows the color composite of the AGN-subtracted HST images. We use the `make_lupton_rgb` function in `Astropy` to produce the images, with F110W in red, F606W in blue, and the average of F110W and F606W in green.

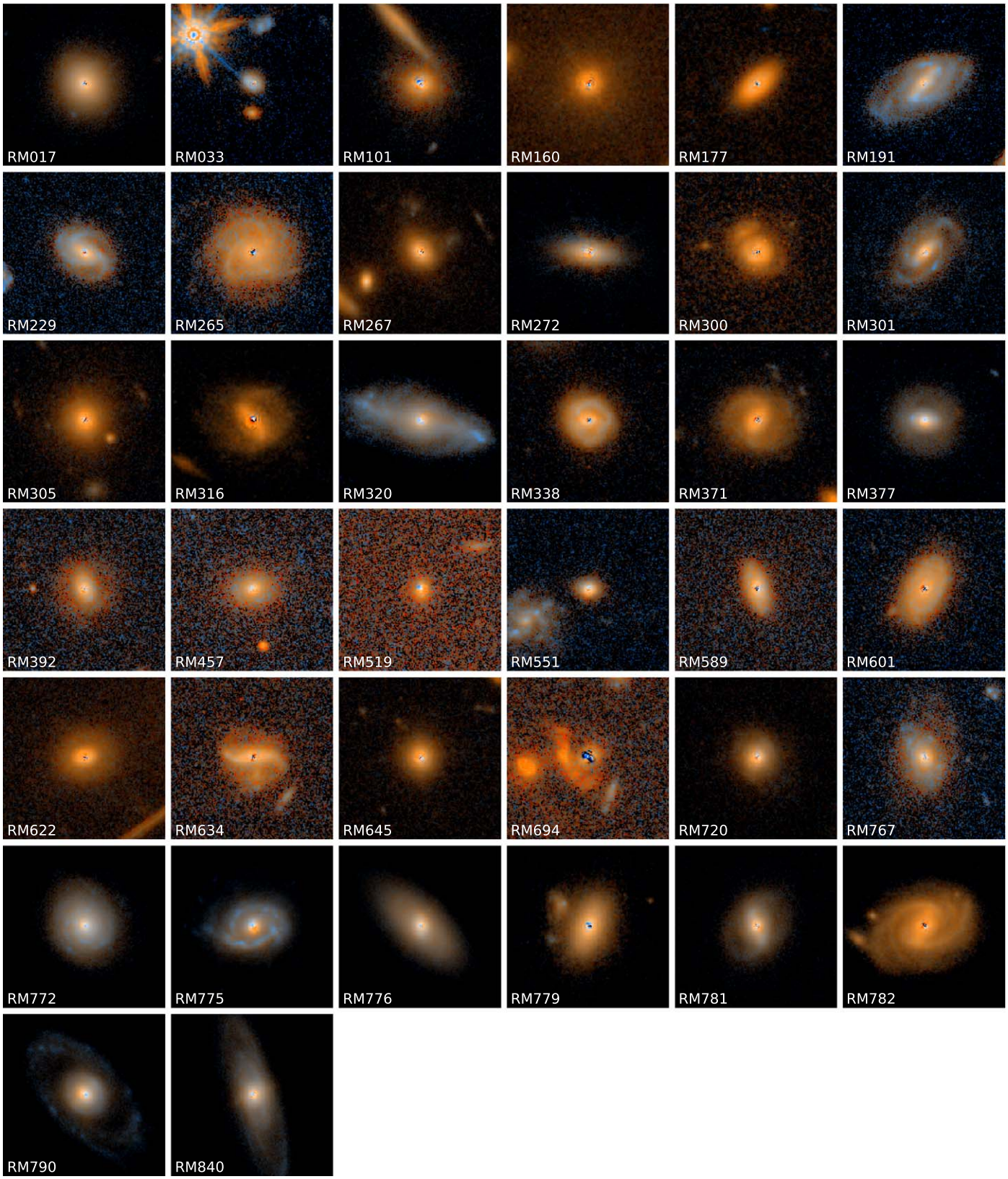

Figure 11. Color-composite images (F110W in red, F606W in blue, and the average of F110W and F606W in green) of the PSF-subtracted host galaxies. The RMIDs are labeled in the lower left corner of each panel, and the images are $7\farcs5 \times 7\farcs5$.

ORCID iDs

Jennifer I-Hsiu Li https://orcid.org/0000-0002-0311-2812
Yue Shen https://orcid.org/0000-0003-1659-7035
Luis C. Ho https://orcid.org/0000-0001-6947-5846
W. N. Brandt https://orcid.org/0000-0002-0167-2453
Catherine J. Grier https://orcid.org/0000-0001-9920-6057
Patrick B. Hall https://orcid.org/0000-0002-1763-5825
Y. Homayouni https://orcid.org/0000-0002-0957-7151
Anton M. Koekemoer https://orcid.org/0000-0002-6610-2048
Donald P. Schneider https://orcid.org/0000-0001-7240-7449
Jonathan R. Trump https://orcid.org/0000-0002-1410-0470

References

Astropy Collaboration, Robitaille, T. P., Tollerud, E. J., et al. 2013, A&A, 558, A33
Bell, E. F., & de Jong, R. S. 2001, ApJ, 550, 212
Bennert, V. N., Auger, M. W., Treu, T., Woo, J.-H., & Malkan, M. A. 2011, ApJ, 742, 107
Bennert, V. N., Treu, T., Ding, X., et al. 2021, ApJ, 921, 36
Bentz, M. C., Denney, K. D., Grier, C. J., et al. 2013, ApJ, 767, 149
Bentz, M. C., & Manne-Nicholas, E. 2018, ApJ, 864, 146
Bernardi, M., Shankar, F., Hyde, J. B., et al. 2010, MNRAS, 404, 2087
Blandford, R. D., & McKee, C. F. 1982, ApJ, 255, 419
Boquien, M., Burgarella, D., Roehlly, Y., et al. 2019, A&A, 622, A103
BradleyL., SipőczB., RobitailleT., et al. (2019) astropy/photutils: v0.6, Zenodo, doi:10.5281/zenodo.2533376
Calzetti, D., Armus, L., Bohlin, R. C., et al. 2000, ApJ, 533, 682
Calzetti, D., Kinney, A. L., & Storchi-Bergmann, T. 1994, ApJ, 429, 582
Comerford, J. M., & Greene, J. E. 2014, ApJ, 789, 112
Davis, M., Guhathakurta, P., Konidaris, N. P., et al. 2007, ApJL, 660, L1
Decarli, R., Falomo, R., Treves, A., et al. 2010, MNRAS, 402, 2453
Di Matteo, T., Springel, V., & Hernquist, L. 2005, Natur, 433, 604
Ding, X., Silverman, J., Treu, T., et al. 2020, ApJ, 888, 37
Ding, X., Silverman, J. D., Treu, T., et al. 2022, ApJ, 933, 132
Ding, X., Treu, T., Birrer, S., et al. 2021, MNRAS, 501, 269
Dong, X. Y., & Wu, X.-B. 2016, ApJ, 824, 70
Du, P., Lu, K.-X., Zhang, Z.-X., et al. 2016, ApJ, 825, 126
Du, P., & Wang, J.-M. 2019, ApJ, 886, 42
Fausnaugh, M. M., Grier, C. J., Bentz, M. C., et al. 2017, ApJ, 840, 97
Ferrarese, L., & Merritt, D. 2000, ApJL, 539, L9
Fonseca Alvarez, G., Trump, J. R., Homayouni, Y., et al. 2020, ApJ, 899, 73
Gao, H., & Ho, L. C. 2017, ApJ, 845, 114
Gebhardt, K., Bender, R., Bower, G., et al. 2000, ApJL, 539, L13
Greene, J. E., Ho, L. C., & Barth, A. J. 2008, ApJ, 688, 159
Greene, J. E., Strader, J., & Ho, L. C. 2020, ARA&A, 58, 257
Grier, C. J., Pancoast, A., Barth, A. J., et al. 2017a, ApJ, 849, 146
Grier, C. J., Shen, Y., Horne, K., et al. 2019, ApJ, 887, 38
Grier, C. J., Trump, J. R., Shen, Y., et al. 2017b, ApJ, 851, 21
Gültekin, K., Richstone, D. O., Gebhardt, K., et al. 2009, ApJ, 698, 198
Habouzit, M., Li, Y., Somerville, R. S., et al. 2021, MNRAS, 503, 1940
Häring, N., & Rix, H.-W. 2004, ApJL, 604, L89
Hastings, W. K. 1970, Biometrika, 57, 97
Heckman, T. M., & Best, P. N. 2014, ARA&A, 52, 589
Homayouni, Y., Trump, J. R., Grier, C. J., et al. 2020, ApJ, 901, 55
Huang, S., Ho, L. C., Peng, C. Y., Li, Z.-Y., & Barth, A. J. 2013, ApJ, 766, 47
Hunter, J. D. 2007, CSE, 9, 90
Into, T., & Portinari, L. 2013, MNRAS, 430, 2715
Jahnke, K., Bongiorno, A., Brusa, M., et al. 2009, ApJL, 706, L215
Jiang, Y.-F., Greene, J. E., & Ho, L. C. 2011a, ApJL, 737, L45
Jiang, Y.-F., Greene, J. E., Ho, L. C., Xiao, T., & Barth, A. J. 2011b, ApJ, 742, 68
Kaspi, S., Maoz, D., Netzer, H., et al. 2005, ApJ, 629, 61
Kelly, B. C. 2007, ApJ, 665, 1489
Khandai, N., Di Matteo, T., Croft, R., et al. 2015, MNRAS, 450, 1349
Kim, M., & Ho, L. C. 2019, ApJ, 876, 35
Kim, M., Ho, L. C., Peng, C. Y., Barth, A. J., & Im, M. 2008, ApJS, 179, 283
Kim, M., Ho, L. C., Peng, C. Y., Barth, A. J., & Im, M. 2017, ApJS, 232, 21
Kinney, A. L., Calzetti, D., Bohlin, R. C., et al. 1996, ApJ, 467, 38
Kormendy, J., & Ho, L. C. 2013, ARA&A, 51, 511
Kroupa, P. 2001, MNRAS, 322, 231
Laor, A. 1998, ApJL, 505, L83
Lauer, T. R., Tremaine, S., Richstone, D., & Faber, S. M. 2007, ApJ, 670, 249
Leitherer, C., Li, I. H., Calzetti, D., & Heckman, T. M. 2002, ApJS, 140, 303
Li, J., Silverman, J. D., Ding, X., et al. 2021a, ApJ, 922, 142
Li, J., Silverman, J. D., Ding, X., et al. 2021b, ApJ, 918, 22
Li, J. I., Shen, Y., Brandt, W. N., et al. 2019, ApJ, 884, 119
Li, J. I., Shen, Y., Ho, L. C., et al. 2021c, ApJ, 906, 103
Lim, P. L., Diaz, R. I., & Laidler, V. 2015, pysynphot: Synthetic photometry software package, Astrophysics Source Code Library, ascl:1303.023
Loeb, A. 2007, PhRvL, 99, 041103
Magorrian, J., Tremaine, S., Richstone, D., et al. 1998, AJ, 115, 2285
Maithil, J., Brotherton, M. S., Shemmer, O., et al. 2022, MNRAS, 515, 491
Maraston, C. 2005, MNRAS, 362, 799
Matsuoka, Y., Strauss, M. A., Shen, Y., et al. 2015, ApJ, 811, 91
McConnell, N. J., & Ma, C.-P. 2013, ApJ, 764, 184
Merloni, A., Bongiorno, A., Bolzonella, M., et al. 2010, ApJ, 708, 137
Metropolis, N., Rosenbluth, A. W., Rosenbluth, M. N., Teller, A. H., & Teller, E. 1953, JChPh, 21, 1087
Molina, J., Wang, R., Shangguan, J., et al. 2021, ApJ, 908, 231
Mutlu-Pakdil, B., Seigar, M. S., Hewitt, I. B., et al. 2018, MNRAS, 474, 2594
Ni, Q., Brandt, W. N., Yang, G., et al. 2021, MNRAS, 500, 4989
Ni, Q., Yang, G., Brandt, W. N., et al. 2019, MNRAS, 490, 1135
Oliphant, T. E. 2006, A guide to NumPy, Vol. 1 (USA: Trelgol Publishing)
Park, D., Woo, J.-H., Bennert, V. N., et al. 2015, ApJ, 799, 164
Peng, C. Y., Ho, L. C., Impey, C. D., & Rix, H.-W. 2010, AJ, 139, 2097
Peng, C. Y., Impey, C. D., Ho, L. C., Barton, E. J., & Rix, H.-W. 2006a, ApJ, 640, 114
Peng, C. Y., Impey, C. D., Rix, H.-W., et al. 2006b, ApJ, 649, 616
Peterson, B. M. 2014, SSRv, 183, 253
Price-Whelan, A. M., Sipőcz, B. M., Günther, H. M., et al. 2018, AJ, 156, 123
Reines, A. E., & Volonteri, M. 2015, ApJ, 813, 82
Schlafly, E. F., & Finkbeiner, D. P. 2011, ApJ, 737, 103
Schlegel, D. J., Finkbeiner, D. P., & Davis, M. 1998, ApJ, 500, 525
Schulze, A., & Wisotzki, L. 2011, A&A, 535, A87
Schulze, A., & Wisotzki, L. 2014, MNRAS, 438, 3422
Sexton, R. O., Canalizo, G., Hiner, K. D., et al. 2019, ApJ, 878, 101
Shangguan, J., Ho, L. C., Bauer, F. E., Wang, R., & Treister, E. 2020, ApJ, 899, 112
Shen, J., Vanden Berk, D. E., Schneider, D. P., & Hall, P. B. 2008, AJ, 135, 928
Shen, Y., Brandt, W. N., Dawson, K. S., et al. 2015a, ApJS, 216, 4
Shen, Y., Greene, J. E., Ho, L. C., et al. 2015b, ApJ, 805, 96
Shen, Y., Grier, C. J., Horne, K., et al. 2023, arXiv:2305.01014
Shen, Y., Horne, K., Grier, C. J., et al. 2016, ApJ, 818, 30
Shen, Y., Hwang, H.-C., Zakamska, N., & Liu, X. 2019, ApJL, 885, L4
Shen, Y., & Kelly, B. C. 2010, ApJ, 713, 41
Shen, Y., & Kelly, B. C. 2012, ApJ, 746, 169
Sijacki, D., Vogelsberger, M., Genel, S., et al. 2015, MNRAS, 452, 575
Silk, J., & Rees, M. J. 1998, A&A, 331, L1
Silverman, J. D., Li, J., & Ding, X. 2022, ApJ, 933, 165
Suh, H., Civano, F., Trakhtenbrot, B., et al. 2020, ApJ, 889, 32
Treu, T., Malkan, M. A., & Blandford, R. D. 2004, ApJL, 615, L97
Volonteri, M., Dubois, Y., Pichon, C., & Devriendt, J. 2016, MNRAS, 460, 2979
Wang, S., Shen, Y., Jiang, L., et al. 2019, ApJ, 882, 4
Waskom, M., Botvinnik, O., O'Kane, D., et al. 2017, mwaskom/seaborn: v0.8.1 (September 2017), v0.8.1, Zenodo, doi:10.5281/zenodo.883859
Woo, J.-H., Treu, T., Barth, A. J., et al. 2010, ApJ, 716, 269
Woo, J.-H., Treu, T., Malkan, M. A., & Blandford, R. D. 2006, ApJ, 645, 900
Woo, J.-H., Yoon, Y., Park, S., Park, D., & Kim, S. C. 2015, ApJ, 801, 38
Yang, G., Brandt, W. N., Alexander, D. M., et al. 2019, MNRAS, 485, 3721
Yesuf, H. M., & Ho, L. C. 2020, ApJ, 901, 42
Yue, M., Jiang, L., Shen, Y., et al. 2018, ApJ, 863, 21
Zhao, Y., Ho, L. C., Shangguan, J., et al. 2021, ApJ, 911, 94
Zhuang, M.-Y., & Ho, L. C. 2020, ApJ, 896, 108
Zibetti, S., Charlot, S., & Rix, H.-W. 2009, MNRAS, 400, 1181